Development of alumina-reinforced elastomeric composites via additive manufacturing

Original Citation:
Development of alumina-reinforced elastomeric composites via additive manufacturing / Barzegar Keyvani, M.. - ELETTRONICO. - (2026).

Availability:
This version is available at http://hdl.handle.net/11589/305001 since: 2026-07-08

Published version
DOI:

Publisher: Politecnico di Bari

Politecnico
di Bari

Department of Mechanics, Mathematics and Management

Mechanical and Management Engineering
Ph.D. Program

Manufacturing Technologies and Systems -
IIND-04/A

Final dissertation

Development of Alumina-Reinforced Elastomeric Composites via Additive Manufacturing

---

by
Majid Barzegar Keyvani
Majid Barzegar

Supervisors:
Prof. Carmine Putignano
Prof. Gianluca Percoco

Coordinator of the Ph.D. Program:
Prof. Giuseppe Casalino

Course XXXVIII, 01/11/2022 - 30/4/2026

Abstract

Vat photopolymerization (VPP) enables the fabrication of high-resolution elastomeric components with complex geometries and excellent surface quality. However, the relatively low mechanical strength and durability of commercially available elastomeric resins limit their broader structural and functional applications. Enhancing mechanical performance while preserving the inherent deformability of elastomeric materials remains a significant challenge, particularly in particle-reinforced systems where filler addition often increases porosity and defect sensitivity.

This thesis investigates the development of alumina-reinforced elastomeric composites fabricated via VPP and examines the influence of filler morphology on processing behavior, microstructural evolution, and mechanical performance. Two alumina morphologies were evaluated: platelet-shaped alumina with a high aspect ratio and sub-micron crushed alumina particles. Composite formulations containing 3 wt.%, 6 wt.%, and 9 wt.% filler were prepared and characterized through rheological analysis, UV–Vis spectroscopy, X-ray diffraction (XRD), scanning electron microscopy (SEM), porosity measurements, tensile testing, hardness measurements, and cyclic loading experiments. The crystallographic texture of the alumina particles within the printed composites was quantified using the Lotgering factor (LF), enabling a direct comparison of morphology-dependent orientation behavior. Platelet-reinforced composites exhibited pronounced preferential alignment during the VPP process, reaching Lotgering factor values of approximately 0.55, whereas sub-micron alumina showed little or no preferred orientation (LF ≈ 0). The platelet systems generally exhibited lower porosity and improved structural consolidation compared with the corresponding sub-micron formulations.

A clear relationship was established between particle morphology, orientation, porosity, and mechanical response. The 3 wt.% platelet-reinforced composite exhibited the best overall performance, increasing the ultimate tensile strength from 12.4 MPa for the neat resin to 45.7 MPa while simultaneously maintaining high deformability and nearly doubling the elongation at break. Cyclic loading experiments further indicated improved retention of mechanical properties at intermediate platelet loadings. In contrast, the sub-micron alumina systems produced only moderate improvements because of limited particle alignment and increased defect sensitivity. The primary contribution of this work is the systematic comparison of platelet-shaped and sub-micron alumina reinforcements under identical VPP processing conditions and the establishment of quantitative correlations between particle morphology, crystallographic orientation, porosity, and mechanical performance. The results demonstrate that platelet-shaped alumina provides a highly effective reinforcement strategy for elastomeric VPP composites and offers practical design guidelines for developing lightweight, compliant, and mechanically robust additively manufactured components for applications such as flexible devices, wearable technologies, energy-absorbing structures, and other advanced engineering systems.

Contents

List of Figures

List of Tables

Chapter 1

Literature Review

1.1 Introduction

Recent advancements have increasingly utilized composite and architected soft materials to address the inherent mechanical limitations of homogeneous polymers. By incorporating functional inclusions within a compliant matrix, it was feasible to independently tailor the stiffness, strength, and actuation behavior. For instance, elastomeric systems with phase-change microstructures demonstrated that microstructural design could significantly enhance the strain capacity and load generation [1]. Similarly, magneto-active composites leveraged controlled particle dispersion and alignment to achieve programmable anisotropy and remote actuation, underscoring the critical role of the microstructure in determining performance [2].

Additive manufacturing, particularly multimaterial and field-assisted printing techniques, facilitates spatial control over the filler distribution, anisotropy, and interfacial bonding. These process–structure–property relationships dictate the mechanical reliability, durability, and actuation precision, demonstrating that the fabrication strategy is integral to the material performance in advanced platforms [3,4]. Studies on the composite soft robots have indicated that raster orientation, layer adhesion, and interfacial continuity significantly influence the tensile strength, flexibility, and failure behavior. These results demonstrate that processing-induced anisotropy and porosity could either enhance or negate the reinforcement effects, depending on the microstructural control [5,6].

Unlike conventional robots, which depend on articulated joints, high-stiffness components, and precise kinematic control, soft robots are primarily constructed from elastomers, gels, and flexible composite materials. These materials facilitated large continuous deformations and intrinsic adaptability. This inherent compliance enables these systems to interact safely with uncertain environments, tolerate positioning errors, and conform to complex geometries without necessitating the exact control of contact forces. Soft robots are more accurately described as continuum systems with distributed deformation rather than assemblies of discrete degrees of freedom. This distinction fundamentally alters the conceptualization of motion, force transmission, and interaction in robotic design [7].

The motivation for these systems is strongly rooted in biological inspiration, wherein living organisms exploit compliant tissues, hierarchical architectures, and distributed actuation to perform complex tasks efficiently. Biological systems, such as octopus arms, worm bodies, and human musculature, demonstrate how compliance enabled dexterous manipulation, smooth locomotion, and controlled force distribution without centralized high-precision control. These systems benefited from "compliance matching" with their environment, reducing stress concentrations at contact interfaces, and enabling safer interactions with humans and fragile objects, particularly in medical, wearable, and collaborative robotic applications [8]. From an embodied intelligence perspective, the physical morphology and material properties of a soft robot could transfer computational complexity from control algorithms to the mechanical body itself, allowing adaptive behavior to emerge from structural and material design rather than explicit command-based control [9].

From a mechanical and materials perspective, the defining feature of these systems is the strong interconnection between material behavior, structural geometry, and functional performance. These systems typically utilized viscoelastic polymers, whose nonlinear deformation, time-dependent response, and damage tolerance were critical for determining actuation efficiency, durability, and load-bearing capacity. These systems were inherently infinite-dimensional and more accurately described using continuum mechanics frameworks rather than rigid-body models, leading to significant challenges in analytical modeling and control. Consequently, stress redistribution, load transfer, and energy dissipation are central design considerations, particularly when reinforcement strategies, fillers, or architected geometries are introduced [10].

Despite substantial progress, these systems continued to face challenges related to the modeling accuracy, fabrication scalability, and performance predictability. The same large deformations and nonlinear material responses that enable adaptability also complicate the control and simulation. Furthermore, many platforms relied on pneumatic or hydraulic actuation, which introduced practical limitations associated with portability, response speed, and system integration [11]. Recent reviews have emphasized that future advances will depend on improved material architectures, integrated sensing strategies, and controlled load-transfer mechanisms that enhance functionality without compromising compliance [12,13].

Soft robotics is fundamentally facilitated by materials whose compliance permitted extensive and continuous deformations and safe interactions with complex environments. In contrast to traditional rigid robots, whose functionality is predominantly determined by kinematic mechanisms and control systems, soft robots derive much of their behavior directly from the intrinsic properties of their materials. A design-oriented definition of soft materials emphasizes that softness is not merely a matter of low elastic modulus but a system-level characteristic emerging from the interaction between the material composition, geometry, and structure [14].

Elastomers and composites are foundational materials of the architectures. Among these materials, silicone-based elastomers, such as polydimethylsiloxane (PDMS) and related formulations, are widely adopted because of their hyperelastic response, processability, and ability to withstand large strains. However, their nonlinear and viscoelastic behaviors, including hysteresis, stress relaxation, and strain-history dependence, strongly influenced actuator repeatability and long-term durability. Therefore, accurate mechanical characterization is essential for the predictive modeling and reliable design of systems operating under cyclic loading conditions [15–18]. Elastomeric inflatable architectures demonstrated how structural reinforcement and geometry could program motion, illustrating that material behavior and design are inseparable in actuation [19,20].

In addition to passive elastomers, smart and stimuli-responsive materials have significantly expanded the capabilities of soft robots. Materials such as dielectric elastomers, shape-memory polymers, liquid crystal elastomers, magneto-active composites, and responsive hydrogels could directly transduce electrical, thermal, optical, and magnetic energy into mechanical deformation. These systems were governed by trade-offs between achievable strain, generated stress, efficiency, and fatigue resistance, which must be balanced for application-specific requirements [21,22]. Flexible actuator technologies further highlighted how thin-film architectures, fiber reinforcement, and multimaterial integration amplified material deformation into controlled robotic motion [23].

Despite rapid progress, several challenges persisted in deploying soft materials for robotic applications. Environmental exposure, mechanical fatigue, and creep could lead to performance degradation, particularly under extreme or prolonged operating conditions . Furthermore, the nonlinear and history-dependent behaviors of soft polymers complicated modeling, sensing integration, and closed-loop control, highlighting the necessity for improved constitutive understanding and material optimization [24].

Recent bioinspired and intelligent frameworks underscored that material intelligence arises from the integration of heterogeneous constituents rather than solely from control strategies, thereby encouraging the widespread adoption of composite soft materials [25]. Comprehensive reviews of bioinspired parts further emphasized that single-material solutions were inherently limited in meeting the combined demands of strength, adaptability, and robustness, establishing composites as a fundamental design strategy in advanced systems [26].

Particle-reinforced elastomers represented a prevalent composite approach for the mechanical and functional properties. Research on magnetically functional composites indicated that reinforcement efficiency is determined by particle size, morphology, and spatial organization rather than filler concentration alone. In these systems, particle alignment and inter-particle interactions predominantly influence stiffness modulation, actuation efficiency, and fatigue behavior, whereas agglomeration and poor dispersion introduced stress concentrations that compromised mechanical performance [27].

Beyond two-phase composites, hierarchical architectures incorporated multiple reinforcing phases have demonstrated superior mechanical tunability and robustness. Three-component elastomer systems illustrated how high-aspect-ratio fibers particle networks, significantly enhanced load transfer and percolation efficiency. These cooperative microstructural interactions enabled large stiffness modulation and improved durability without sacrificing compliance, highlighting the importance of microstructural synergy in composite soft materials [28].

Fiber-based reinforcement offered an effective means of introducing anisotropy and directional stiffness into soft matrix structures. Both theoretical and experimental studies indicated that the reinforcement efficiency was critically dependent on the fiber aspect ratio, orientation, and volume fraction. Optimization-driven designs had demonstrated that strategically aligned fibers outperform isotropic composites at comparable filler contents, confirming that microstructural alignment is a primary determinant of the mechanical performance of soft composites [29].

Interfacial mechanics played a decisive role in governing the performance and failure of composite soft materials. Weak interfaces promoted debonding and void nucleation, whereas strong interfacial adhesion enabled progressive failure and enhanced fatigue resistance, underscoring the interface-dominated nature of reinforcement in soft composites [30].

Fabric-reinforced elastomers exemplified the impact of microstructural reinforcement on the alteration of failure modes in soft materials. Empirical investigations of fabric–silicone composites had revealed that woven architectures introduce multistage failure mechanisms and enhance tear resistance, thereby transforming highly compliant elastomers into load-bearing soft structures [31]. Factors such as alignment, aspect ratio, interfacial bonding, and defect suppression collectively determine the load transfer, durability, and functional performance of particle-, fiber-, and hybrid-reinforced systems. This microstructure-driven framework forms the foundation for advanced composite design in systems and directly informs the experimental investigations of filler morphology, alignment, and porosity control, as presented in the following chapters [32]. Functional fiber architectures, including aligned, twisted, and hierarchically assembled fibers, facilitate programmable anisotropy and reduce the reliance on complex control strategies by embedding mechanical intelligence directly into the material system. This perspective redefined reinforcement as a structural and systemic design tool rather than a mere enhancement of stiffness, underscoring the critical role of fiber orientation, continuity, and interfacial coupling in determining macroscopic performance [33]. The effectiveness of continuous fiber reinforcement is further exemplified in ultra-robust soft actuators that integrate high-strength carbon fibers with thermoplastic matrices. Bilayer and laminated composite architectures exploited extreme anisotropy in thermal expansion and elastic modulus to achieve large, programmable deformations while maintaining exceptional load-bearing capability. In such systems, the continuity and alignment of carbon fibers were important to both mechanical robustness and actuation performance, enabling multi-stimulus responses (thermal, optical, and electrical) without compromising durability. [34].

Functional reinforcement further extended the role of composites in mechanical enhancement. Studies of hard-magnetic soft materials indicated that particle-filled elastomers facilitate programmable shape morphing and remote actuation, with performance governed by particle distribution, alignment, and matrix stiffness. Similarly, flexible sensing materials depend on percolating filler networks, whose electromechanical response is dictated by microstructural connectivity and interfacial stability [35,36]. Processing-induced defects, particularly porosity, consistently emerge as a predominant factor limiting reinforcement efficiency. Researches on natural-fiber and printed biocomposites demonstrated that void networks formed during extrusion and curing significantly reduce strength, fatigue life, and interfacial load transfer [37].

Soft robotics relies on compliant and deformable materials to achieve adaptable motion and safe interaction with complex environments; however, these advantages come with considerable material performance challenges. Flexible polymers, such as silicones, elastomers, and hydrogels, commonly used in actuators and structures, often exhibit limited mechanical properties, low tensile strength and vulnerability to damage under repetitive loading conditions, restricting their operational lifetime and load-bearing capacity in real-world tasks [38,39]. Hybrid material systems that combine soft and stiff features have been explored to enhance mechanical properties and enable complex functionality [40].

Additive **M**anufacturing (AM), particularly **V**at **P**hoto**p**olymerization (VPP), has rapidly expanded the ability to produce fine polymer components with great surface finish and geometric accuracy. Despite these advantages, standard VPP resins remain brittle and mechanically weak, limiting their use in demanding structural applications. So, researchers have increasingly investigated polymer nanocomposites that have very small amounts of inorganic nanoparticles to improve durability without sacrificing printability [41].

For example, Ávila-López et al. demonstrated that adding 0.4 wt.% of TiO_2 with a primary particle size of approximately 25 nm to VPP resins can significantly improve compressive strength, toughness and frictional performance, unlocking possibilities for lightweight components in field of automotive engineering [42]. Similarly, Domun et al. enhanced the toughness of epoxy systems using plasma-functionalized graphene nanoplatelets, overcoming challenges related to the brittleness of epoxy. Other researchers have investigated slurry behavior in photopolymer-ceramic systems [43]. Ryu et al. demonstrated that the size of alumina particles critically influences the viscosity, sedimentation and curing performance in VPP, ultimately effecting printability and dimensional accuracy [44]. Wang et al. presented a different strategy by forming a double interpenetrating polymer network within an epoxy-clay composite, improving both the tensile and fracture properties through better interaction and dispersion of clay platelets [45]. Domun et al. similarly reviewed how a range of nanomaterials can enhance epoxy systems, stressing that uniform dispersion and strong bonding are essential for achieving these improvements [46].

Xu et al. utilized modified nanoclay particles to strengthen cardanol-based systems, showing that improved dispersion and chemically active interfaces are key to significantly better performance [47]. In fiber-reinforced Systems, Kaybal et al. demonstrated that adding small amounts of alumina nanoparticles can substantially enhance the impact resistance of carbon-fiber composites by improving the crack-deflection mechanisms and fiber-matrix adhesion [48]. Senthil Kumar et al. studied similar improvements in hybrid natural-fiber composites, presenting that alumina fillers can increase stiffness, strength and hardness when well-distributed [49].

Sabarinathan et al. showed that even untreated waste particles can improve the mechanical properties such as hardness and thermal behavior, although the monitoring of the process is required to avoid particle agglomeration [50]. Rosenberger et al. investigated strategies to orient alumina platelets during additive manufacturing, inspired by natural materials like nacre that apply aligned microstructures for toughness [51]. Yousri et al. dopped very low loadings of alumina nanoparticles to epoxy coatings and demonstrated that even 0.25 wt.% can meaningfully enhance hardness, tensile behavior and water resistance when dispersion is well controlled [52]. Others, such as Myles et al., have focused on platelet orientation during printing, showing that shear-induced alignment in VPP systems can be achieved without external fields, enabling bio-inspired ceramic architecture [53]. Complementing this, Parameswaran et al. examined how alumina particle size and loading influence the mechanical and thermal properties of epoxy, highlighting the importance of optimizing filler characteristics to balance toughness and stiffness [54].

Other researchers, such as Shukla and Hulka, have extensively studied ultra-thin alumina platelets (approximately 200 nm thick) as reinforcements for epoxy. Their work demonstrated that high-aspect-ratio platelets can dramatically influence fracture behavior, stiffness and strength, particularly when their dispersion and volume fraction are carefully controlled [55–57].

While soft robotics provides an important application context, the central scientific focus of this thesis is the development of alumina-reinforced elastomeric composites manufactured via vat photopolymerization. Therefore, the following sections focus on the relationships between particle morphology, processing, microstructure, and mechanical performance that govern the behavior of these materials.

1.2 Research Gap and Scientific Motivation

Previous studies have demonstrated that ceramic fillers can improve the stiffness, hardness, and strength of polymer composites. However, most investigations have focused on thermoset or thermoplastic matrices, while elastomeric photopolymer systems processed via vat photopolymerization (VPP) remain comparatively underexplored. Furthermore, although particle alignment and high-aspect-ratio reinforcements have been widely investigated in ceramic processing and rigid composite systems, the influence of filler morphology on particle orientation, porosity evolution, and mechanical performance in elastomeric VPP composites has not been systematically studied. In particular, a direct comparison between platelet-shaped and sub-micron alumina fillers processed under identical VPP conditions has not been reported. Therefore, the relationship between particle morphology, crystallographic orientation, porosity, and mechanical performance remains insufficiently understood. This thesis addresses this gap through the development and characterization of alumina-reinforced elastomeric composites fabricated by VPP.

In addition to the limited understanding of morphology-dependent reinforcement in elastomeric VPP composites, there remains a lack of quantitative studies linking processing-induced microstructural features to the resulting mechanical behavior. Previous investigations have typically reported mechanical property improvements following filler addition but have rarely established direct relationships between particle morphology, preferential orientation, porosity evolution, and tensile performance within a unified experimental framework. Furthermore, the influence of crystallographic texture on the reinforcement efficiency of ceramic-filled elastomeric photopolymers has received little attention, despite its potential importance for load transfer and structural integrity. Consequently, the mechanisms through which particle morphology affects consolidation and mechanical response in VPP-printed elastomer composites remain insufficiently understood. Addressing these limitations requires a systematic experimental approach that combines microstructural characterization with mechanical evaluation under identical processing conditions.

1.3 Originality and Scientific Contribution

Platelet-shaped and sub-micron alumina particles were intentionally selected to investigate the role of particle morphology on reinforcement behavior in elastomeric VPP composites. The platelet particles possess a high aspect ratio and are expected to exhibit preferential alignment during layer-by-layer photopolymerization, potentially enhancing load transfer and reducing defect sensitivity. In contrast, the sub-micron crushed alumina particles exhibit a near-equiaxed morphology and provide a reference system with limited orientation effects. By comparing these two morphologies under identical processing conditions, the present study isolates the influence of particle shape on rheological behavior, particle orientation, porosity development, and mechanical performance. To the best of the author's knowledge, such a systematic morphology-based comparison has not been previously reported for elastomeric alumina-reinforced composites fabricated via vat photopolymerization.

Despite extensive research on ceramic and nanoparticle reinforcement in rigid epoxy systems, enhancing the strength without compromising ductility remains a significant challenge in elastomeric VPP materials. In soft matrices, the addition of fillers often results in increased defect sensitivity and porosity and reduced extensibility. Although particle alignment has been extensively studied in ceramic processing, its role in elastomeric photopolymer systems fabricated via VPP has received limited attention. This study investigated the influence of filler morphology on the orientation, consolidation, and mechanical performance of VPP-printed elastomer composites. Elastomeric nanocomposites were fabricated by incorporating i) platelet-shaped and ii) sub-micron crushed alumina particles at a loading of 3 wt.%, 6 wt.%, and 9 wt.%. The rheological behavior of alumina-incorporated photopolymer resins used for VPP and the mechanical performance of printed nanocomposites (e.g., tensile strength, fracture elongation, and cyclic loading behavior) were examined. The reinforcement mechanisms were analyzed based on the morphology and concentration of the alumina fillers. By quantifying the crystallographic texture using the Lotgering factor, we compared the morphology-dependent behavior under identical processing conditions. The results established a clear relationship between the particle shape, orientation, porosity, and tensile response.

The novelty of this work lies in the systematic comparison of platelet-shaped and sub-micron alumina fillers processed under identical VPP conditions and in the establishment of quantitative relationships between particle morphology, preferential orientation (Lotgering factor), porosity, and mechanical performance. Unlike previous studies that primarily focused on rigid thermoset systems or filler loading effects, the present work demonstrates how particle morphology governs reinforcement efficiency in elastomeric VPP composites, providing design guidelines for achieving improved strength while preserving deformability.

Although alumina-reinforced polymer composites have been widely investigated in thermoplastic matrices such as PLA, PA12, and polypropylene [46], their implementation in VPP processes has received comparatively limited attention. In particular, the influence of filler morphology on particle orientation, porosity evolution, and the simultaneous improvement of strength and ductility in soft photopolymer matrices has not yet been systematically explored. Alumina was selected as the reinforcing phase because of its high stiffness, excellent thermal stability, and favorable compatibility with polymeric materials. Nevertheless, despite extensive studies on ceramic and nanoparticle reinforcement in rigid epoxy-based systems [55–57], enhancing mechanical strength while preserving ductility remains a major challenge for elastomeric materials processed by VPP. In compliant polymer matrices, the addition of fillers can increase defect sensitivity, promote porosity formation, and reduce elongation at break [50]. Moreover, although the effect of particle alignment has been extensively investigated in ceramic processing, its influence on elastomeric photopolymer composites fabricated through VPP remains insufficiently understood. Accordingly, the present study examines the role of alumina particle morphology in governing particle orientation, structural consolidation, and the resulting mechanical performance of VPP-printed elastomeric composites. Such materials are of particular interest for applications including flexible actuators, wearable technologies, and energy-absorbing structures, where the combination of high deformability and enhanced mechanical robustness is of critical importance [54].

Chapter 2

Materials, Processing and Experimental Methods

In this study, elastomeric nanocomposites were fabricated by doping platelet-shaped and submicron alumina particles at loadings of 3 wt.%, 6 wt.%, and 9 wt.%. The rheological behavior as well as the optical properties of the Al_2O_3-incorporated photopolymer resins used for VPP and the mechanical performance of the printed nanocomposites (e.g., tensile strength, fracture elongation and cyclic loading behavior) were investigated. The reinforcement mechanisms were discussed with respect to the morphology and concentration of the alumina fillers.

2.1 Material and experimental methods

The acrylate-based photocurable resin utilized in this study was **Ela**stomer Resin Grade **400** (ELA400, Phrozen Inc., Taiwan). The resin consisted of a copolymer based on urethane acrylate and a vinyl-functionalized reactive diluent optimized for VPP. Its high reactivity is attributed to radical reactions. According to the manufacturer's specifications, the unfilled printed elastomer presented a superior fracture elongation of 300% (ASTM D412). Two types of alumina fillers were incorporated: ***i***) single-crystal platelet-shaped alumina (RonaFlair White Sapphire, Merck KGaA, Germany; thickness: ~100 nm, diameter: ~5 µm;) and ***ii)*** sub-micron alumina particles (CT3000SG, Almatis GmbH, Ludwigshafen, Germany; d_{10}: ~0.43 µm, d_{50}: ~0.51 µm and d_{90}: ~0.60 µm) [58].

VPP resins were prepared by loading the ELA400 matrix with either platelet-shaped or sub-micron alumina particles at concentrations of 3 wt.%, 6 wt.%, and 9 wt.%. After adding the alumina particles, the mixture was homogenized using a tumbling mixer (Turbula®, Willy A. Bachofen AG, Basel, Switzerland). Alumina milling balls were added to enhance the homogeneous dispersion of alumina filler particles within the resin. The mixing was conducted at 72 rpm for 24 h under ambient conditions. The dispersion quality of the particles in the resin was qualitatively examined using SEM observations of the printed composites, allowing evaluation of their distribution and agglomeration behavior. No noticeable sedimentation occurred during processing, presumably owing to the relatively high viscosity of the filled formulations and the continuous homogenization applied prior to the printing process. Following homogenization, the filled resins were processed using VPP with a desktop 3D printer with UV wavelength of 405 nm with the intensity of the 3.72 $\mathrm{mW/cm^2}$ (Elegoo Saturn 1, Elegoo Inc., China). Printing was operated with a layer thickness of 0.1 mm and an exposure time of 15 s per layer. This process was selected to ensure consistent geometry and smooth surface for mechanical testing. Dog-bone specimens conforming to “ISO 37 Type 4” dimensions. This geometry was chosen for its suitability in tensile and cyclic loading behavior of polymer-based materials. Post-curing was performed under UV light in a curing chamber (Elegoo Mercury Plus V2.0, Elegoo Inc., China) for 1 h at room temperature to ensure full polymerization (**Figure 1**).

Optical characterization was operated using a UV-Vis spectrophotometer (UV-2700, Shimadzu, Japan). Transmission spectra were collected from 300 nm – 800 nm at 300 nm/min with a 1 nm bandwidth, using ethanol as a baseline.

The particle morphology of the alumina fillers was analyzed using a **S**canning **E**lectron **M**icroscope (SEM, Gemini 2, Carl Zeiss Microscopy GmbH, Oberkochen, Germany). Additionally, the crystallographic texture of alumina in ELA400 was investigated using a Philips **X-r**ay **d**iffractometer (XRD, Philips Analytical, Almelo, The Netherlands). XRD analysis enabled the determination of the **L**otgering **F**actor (LF) of the alumina particles within the composite [59–61].

The Lotgering factor represents the degree of preferred crystallographic orientation by comparing the relative intensities of selected diffraction peaks in the textured sample with those of a randomly oriented reference powder. An LF value of 0 corresponds to a completely random orientation, whereas a value of 1 indicates perfect alignment along the selected crystallographic planes. The randomly oriented reference intensities (I_0) were obtained from the XRD pattern of the corresponding alumina powder prior to incorporation into the resin. The LF was calculated according to::

$$LF = \frac{P - P_0}{1 - P_0} \tag{2.1}$$

where

$$P = \frac{\sum I(hkl)_{preferred}}{\sum I(hkl)_{total}}, P_0 = \frac{\sum I_0(hkl)_{preferred}}{\sum I_0(hkl)_{total}} \tag{2.2}$$

Here, $I(hkl)$ represent the measured intensities of the preferred orientation peaks and $I_0(hkl)$ corresponds to the intensities from a randomly oriented powder reference. The LF ranged from 0 (random orientation) to 1 (perfect alignment).

Porosity was calculated to evaluate the quality of consolidation and the effect of filler loading and particle morphology on void formation during the curing process. These measurements were used to correlate the microstructural defects with the mechanical performance and reinforcement efficiency of the composites. The porosity is calculated as

$$\text{Porosity} = 1 - \frac{\rho}{\rho_0} \tag{2.3}$$

here, ρ and ρ_0 represent the measured and the theoretical density, respectively. The measured density was determined from the measured mass and geometric volume of each specimen, whereas the theoretical density was calculated using the rule of mixtures based on the densities and weight fractions of the elastomer matrix and alumina filler.

Rheological characterization was performed using a rotational rheometer (MCR 702e, Anton Paar, Austria) equipped with a parallel plate geometry and a 1 mm measuring gap to investigate the influence of alumina morphology and filler loading on the flow behavior of the photocurable resins used for VPP. Oscillatory rheological measurements were conducted at 25 °C. The complex viscosity (η*) was determined from frequency sweep experiments performed at 1 Hz and 1% strain. The storage modulus (G′), which represents the elastic energy stored during deformation, and the loss modulus (G″), which represents the viscous energy dissipated during deformation, were obtained from oscillatory measurements. Hardness measurements were performed using a Zwick Shore A hardness tester (Bareiss Prüfgerätebau GmbH, Germany).

Mechanical characterization was performed at 25 °C. Shore A hardness measurements were carried out in accordance with ASTM D2240, while tensile properties, including ultimate tensile strength and elongation at break, were determined using a universal testing machine (Coesfeld Materialtest GmbH, Dortmund, Germany) operated at a crosshead speed of 25 mm/min following ASTM D412. The yield strength was defined as the stress corresponding to the first discernible deviation from the initial quasi-linear elastic portion of the stress–strain curve. The cyclic mechanical behavior was evaluated under tensile loading using an Instron 5564 universal testing machine (Instron, USA) at room temperature. Tests were conducted under stress-controlled conditions with a constant amplitude ranging from 0 to 12 MPa at a frequency of 1 Hz for 100 loading cycles, while the corresponding strain response was continuously monitored. It should be noted that the relatively small number of loading cycles and the limited sample size restrict the ability to draw definitive conclusions regarding long-term cyclic loading behavior. Moreover, the adopted protocol does not fully comply with standardized cyclic loading procedures, and parameters such as loading frequency and stress amplitude were not systematically optimized according to established standards. Consequently, the results should be regarded as preliminary and comparative, providing qualitative insights into the cyclic mechanical response rather than a comprehensive assessment of cyclic loading behavior. Following cyclic loading, the specimens were subjected to tensile testing under the same ASTM D412 conditions to evaluate the influence of cyclic deformation on their mechanical properties. In addition, the effect of print orientation on tensile strength and Shore A hardness was investigated using the optimized alumina formulation. Specimens with different build orientations were fabricated via vat photopolymerization (VPP), and their mechanical performance was subsequently evaluated through tensile and hardness testing.

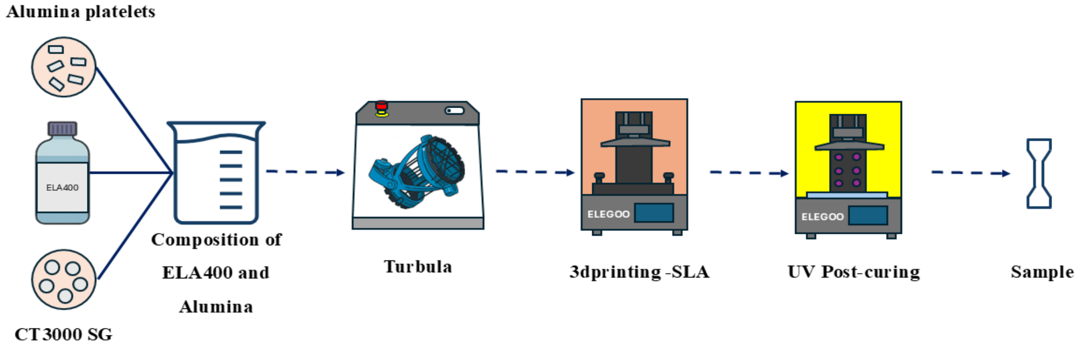

Figure 1: Schematic of the preparation, fabrication, and post-processing of alumina-reinforced elastomers. During preparation, two types of powder (platelet-shaped alumina and CT3000SG) were mixed with ELA400. The samples were then printed using the Elegoo Saturn 1 and finally post-cured for 1 h.

2.2 Statistical Analysis

Experimental data are reported as mean ± standard deviation, where applicable, for tensile, hardness, porosity, and cyclic loading measurements. Unless otherwise stated, at least three independently fabricated specimens were prepared and tested for each composition for mechanical and porosity characterization. Rheological measurements and XRD analyses, including Lotgering factor calculations, were performed as representative measurements for the corresponding printed formulations. No data transformation, normalization, or outlier removal procedures were applied before analysis. As the primary objective of this study was the comparative evaluation of material performance, inferential statistical analyses and post-hoc hypothesis testing were not conducted. The reported standard deviations represent the experimental variability arising from specimen fabrication and testing. Data analysis and graphical representation were performed using OriginPro 2025 (OriginLab Corporation, Northampton, MA, USA).

The reported standard deviations provide an indication of experimental scatter and repeatability for the investigated formulations. In general, the variability observed within each formulation was generally smaller than the differences observed between formulations, particularly for tensile strength, elongation at break, and hardness. Therefore, the observed performance trends are considered representative of the effect of filler morphology and loading. However, due to the limited number of specimens and the exploratory nature of this study, formal inferential statistical analyses, such as analysis of variance (ANOVA), were not performed. Consequently, the results should be interpreted as comparative trends rather than statistically significant differences in the strict inferential sense.

2.3 Printed dog bone samples

Dog-bone specimens (**Figure 2**) conforming to “ISO 37 Type 4” dimensions (total length: 35 mm, head width: 6 mm ± 0.5 mm, neck width 2 mm ± 0.1 mm, thickness 1 mm ± 0.1 mm, and initial gauge length: 10 mm ± 0.5 mm) were fabricated using VPP with a desktop 3D printer with UV wavelength of 405 nm with the intensity of the 3.72 mW/cm^2 (Elegoo Saturn 1, Elegoo Inc., China). Printing was operated with a layer thickness of 0.1 mm and an exposure time of 15 s per layer. This process was selected to ensure consistent geometry and smooth surface for mechanical testing. This geometry was chosen for its suitability in tensile and cyclic loading behavior of polymer-based materials. Post-curing was performed under UV light in a curing chamber (Elegoo Mercury Plus V2.0, Elegoo Inc., China) for 1 h at room temperature to ensure full polymerization.

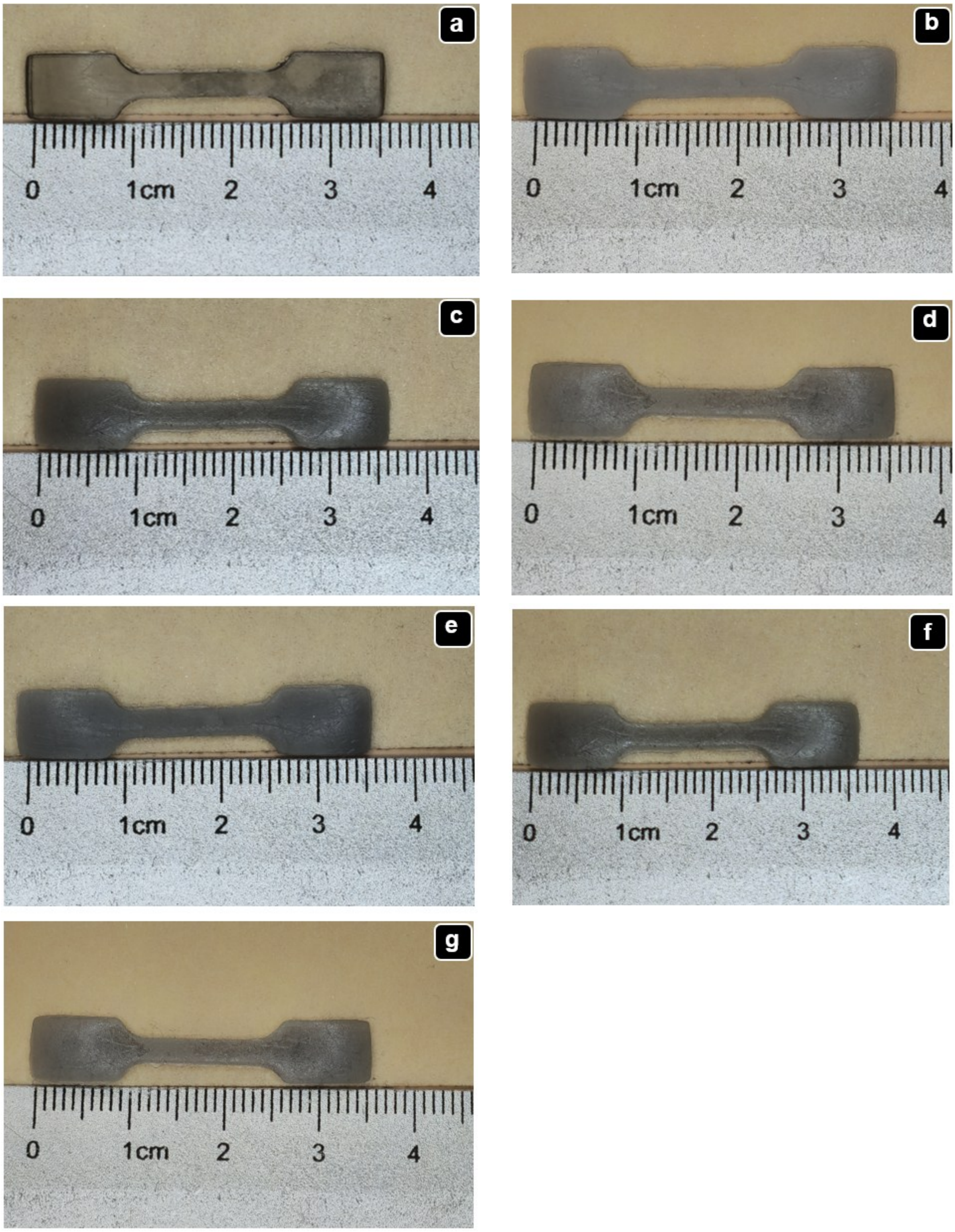

Figure 2: Printed dog-bone specimens based on ISO 37 Type 4: (a) neat ELA400; (b–d) platelet-reinforced composites containing 3 wt.%, 6 wt.%, and 9 wt.% alumina; and (e–g) sub-micron alumina-reinforced composites containing 3 wt.%, 6 wt.%, and 9 wt.% alumina. The dimensional shrinkage in all specimens was less than 5%.

Chapter 3

Microstructure-Property Relationships in Alumina-Reinforced VPP Composites

3.1 The particle morphology of Alumina Powders

The SEM image revealed that the alumina platelets appear as thin, flat flakes with irregular and angular shapes (**Figure 3 a**). Their morphology is characterized by a high aspect ratio with large lateral dimensions compared to their thickness (thickness: ~100 nm with lateral dimensions of several micrometers). In contrast, the CT3000SG powder (**Figure 3 b**) comprised rounded micron-scale particles that aggregated into compact clusters with rough and faceted surfaces, which are typical features of sintered micro - alumina. This morphology facilitates the formation of three-dimensional structures when incorporated into the resin (low aspect ratio, d10: ~0.43 µm, d50: ~0.51 µm and d90: ~0.60 µm). Additionally, these particles represented a dense and compact structure, indicating a high degree of crystallinity typical of α-phase alumina.

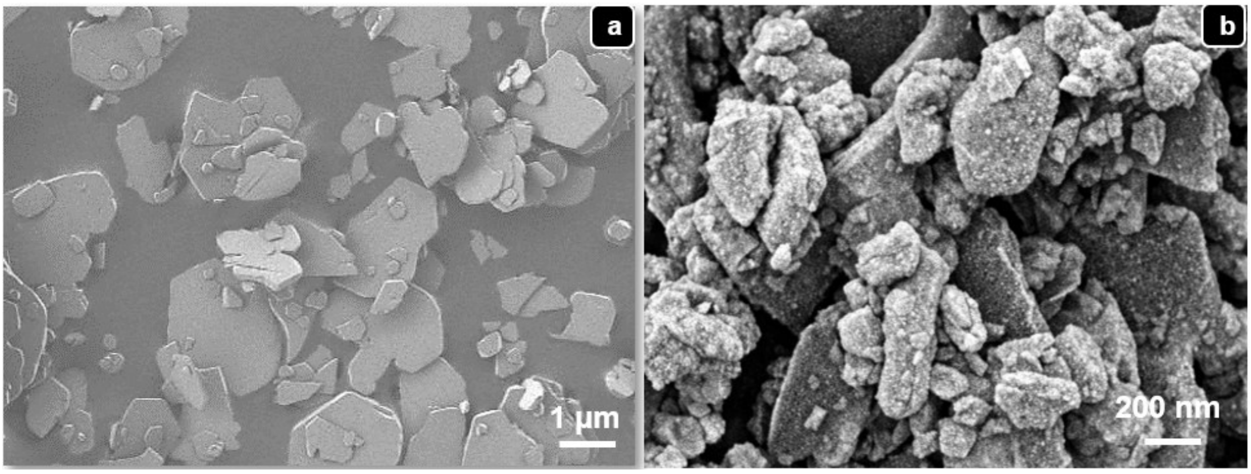

Figure 3: SEM micrographs of alumina powders illustrating particle morphology and size distribution, acquired using a Gemini 2 microscope: (a) platelet-shaped alumina with a high aspect ratio and a thickness of approximately 100 nm, with lateral dimensions of several micrometers; and (b) CT3000SG alumina with a low aspect ratio ($d_{10} \approx$ 0.43 µm, $d_{50} \approx$ 0.51 µm, and $d_{90} \approx$ 0.60 µm).

Elemental mapping through **E**nergy-**d**ispersive X-ray **S**pectroscopy (EDS) further confirmed the distribution of the alumina fillers within the composite (**Figure 4**). The correlation between the aluminium and oxygen measurements confirmed that the identified particles were Al_2O_3 particles. The absence of extraneous elements indicates that the composite comprised only the intended constituents.

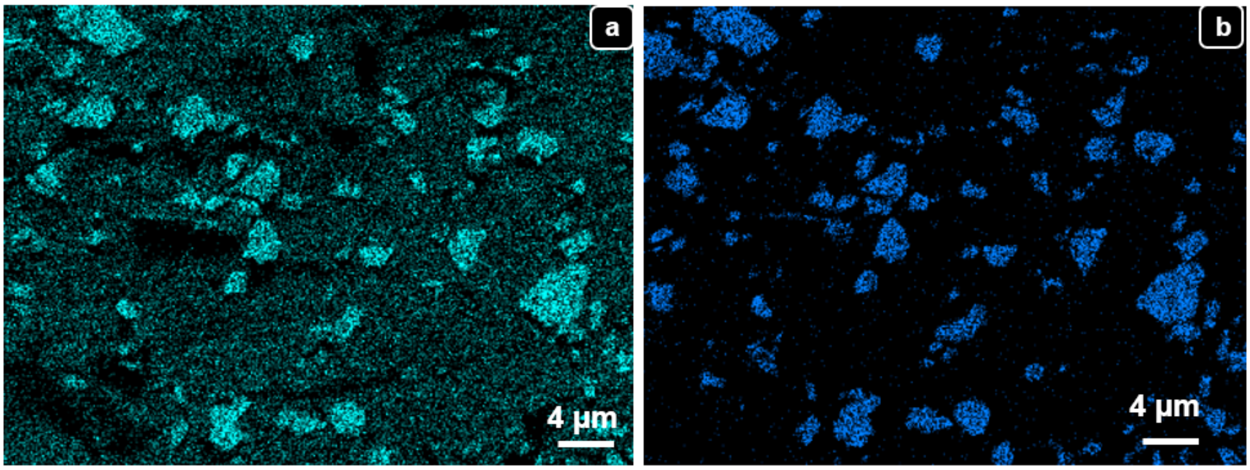

Figure 4: EDS elemental maps of alumina powders acquired using a Gemini 2 microscope, showing the distribution of (a) aluminum and (b) oxygen. No additional elemental species were detected within the analyzed particles.

3.2 The Optical Properties of the Composites

The UV-Vis transmission spectra of ELA400 and composites containing different loadings of platelet and sub-micron fillers in the 300 nm – 800 nm wavelength range are presented in **Figure 5**. The highest optical transparency was observed for ELA400, with a transmission of approximately 83.9% at 405 nm and a consistently high transmission across the visible region. With increasing platelet content, a gradual decrease in transmission was observed, from 67.3% at 3 wt.% to 48.7% and 52.3% at 6 wt.% and 9 wt.%, respectively, which was attributed to enhanced light scattering and absorption. In contrast, a pronounced reduction in optical transmission was observed upon the incorporation of sub-micron fillers, even at low loadings, with only 17.8% transmission at 3 wt.%, further decreasing to 15.6% and 10.4% at 6 wt.% and 9 wt.%, respectively. A strong dependence of optical transparency on both filler size and concentration was demonstrated, with sub-micron fillers having a significantly more detrimental effect than platelet fillers.

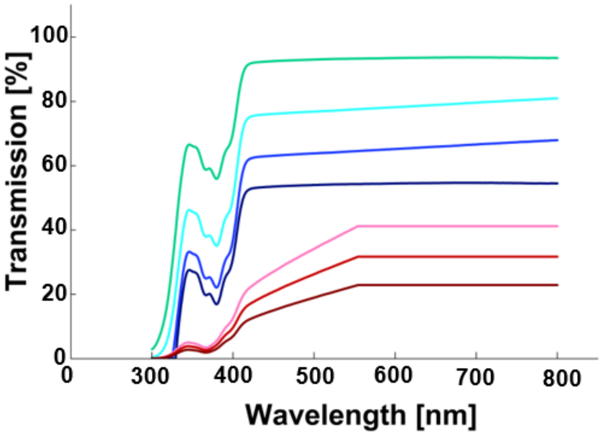

Compositions	405 nm
ELA400	83.9%
ELA + 3 wt.% Platelets	67.3%
ELA + 6 wt.% Platelets	48.7%
ELA + 9 wt.% Platelets	52.3%
ELA + 3 wt.% Sub-micron	17.8%
ELA + 6 wt.% Sub-micron	15.6%
ELA + 9 wt.% Sub-micron	10.4%

Figure 5: **UV–Vis transmittance spectra (300–800 nm) of ELA400 resins containing alumina reinforcements at concentrations of 3 wt.%, 6 wt.%, and 9 wt.%. The reported UV–Vis transmittance values correspond to representative measurements of the printed compositions.**

According to the calculation of the **C**ritical **E**nergy (E_c) and **P**enetration **D**epth (D_p) using the Jacobs working curve [62], ELA400 exhibited (**Table 1**) the highest critical energy, approximately 68 $\mathrm{mJ/cm^2}$, signifying that it requires the least energy to initiate polymerization. In contrast, platelet-filled systems moderately decreased E_c, ranging from 27 $\mathrm{mJ/cm^2}$ to 49 $\mathrm{mJ/cm^2}$, due to enhanced scattering that facilitates light distribution within the resin. The sub-micron fillers exerted the most pronounced effect at a concentration of 6 wt. % and 9 wt.%, E_c decreased ranging from 26.4 $\mathrm{mJ/cm^2}$ to 10 $\mathrm{mJ/cm^2}$. However, these sub-micron systems also presented the lowest D_p, indicating stronger attenuation of light within the resin and a reduced cure depth despite their lower Ec values.

Table 1: Comparison of D_p and E_c across platelet and sub-micron alumina-reinforced resins at concentrations of 3 wt.%, 6 wt.%, and 9 wt.%.

Compositions	D_p [mm]	E_c [mJ/cm²]
ELA	1.2	67.7
ELA + 3 wt.% Platelets	0.6	48.6
ELA + 6 wt.% Platelets	0.4	27.4
ELA + 9 wt.% Platelets	0.3	27.6
ELA + 3 wt.% Sub-micron	0.6	51.6
ELA + 6 wt.% Sub-micron	0.4	26.4
ELA + 9 wt.% Sub-micron	0.3	10.0

* Values are presented as representative D_p and E_c results for the corresponding compositions.

The FTIR spectra of the ELA400 resin exhibited peaks associated with acrylate functional groups, including a strong $\mathrm{C{=}O}$ stretching vibration at approximately 1720 $\mathrm{cm^{-1}}$, $\mathrm{C{-}O}$ stretching near 1150 $\mathrm{cm^{-1}}$, and $\mathrm{C{-}H}$ stretching in the region of 2850 $\mathrm{cm^{-1}}$ - 2950 $\mathrm{cm^{-1}}$. These peaks correspond to the polymer backbone and are consistent with the photopolymer formulation used in the VPP. The broad peak observed around 3400 $\mathrm{cm^{-1}}$ can be attributed to $\mathrm{O{-}H}$ stretching, indicating slight moisture absorption or residual hydroxyl groups.

When alumina fillers were doped, some noticeable shifts and changes in peak intensities occurred, especially at 1100 $\mathrm{cm^{-1}}$ - 1000 $\mathrm{cm^{-1}}$ and 1700 $\mathrm{cm^{-1}}$ - 1750 $\mathrm{cm^{-1}}$, indicating physical and possibly weak chemical interactions between the ceramic particles and polymer matrix. For the micro-powder composites, increasing filler content from 3 wt.% to 9 wt.% resulted in a gradual decrease in transmittance intensity and a slight broadening of the carbonyl band, suggesting restricted polymer chain movement due to filler incorporation. (**Figure 6**).

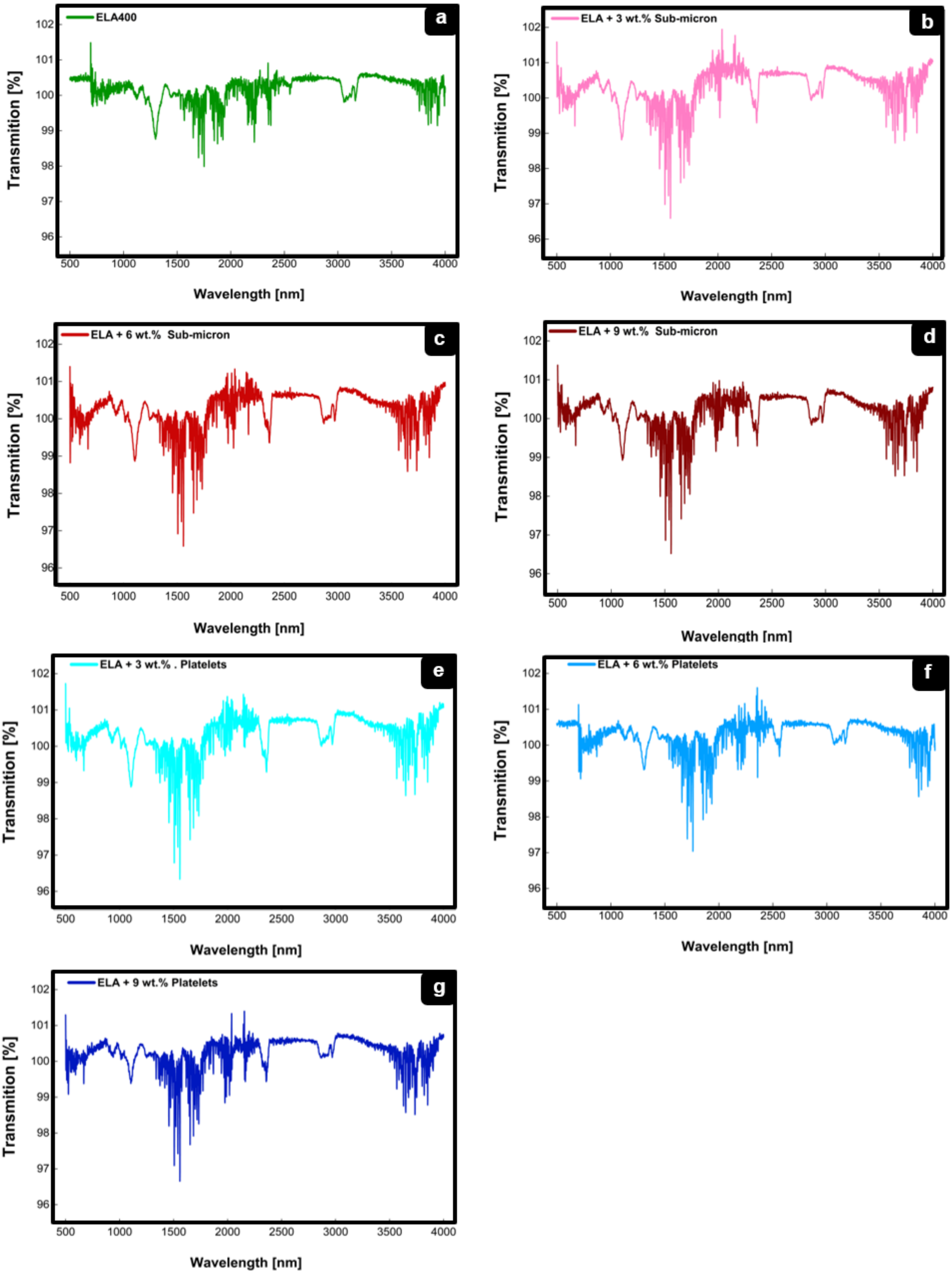

Figure 6: FTIR spectra of alumina-reinforced elastomer composites containing 3 wt.%, 6 wt.%, and 9 wt.% alumina. The presented spectra correspond to representative measurements of the printed compositions.

3.3 The Rheological Properties of the Composites

The rheological results showed that the loss modulus (G″) remained higher than the storage modulus (G′) for all investigated formulations, indicating that the ELA-alumina suspensions exhibited predominantly viscous behavior at 25 °C (**Figure 7**). The relatively low G′ values suggest the presence of a weak elastic network, which is typical of uncured photopolymer resins. The addition of 3 wt.% platelet-shaped alumina increased both G′ and G″ compared with the neat ELA400 resin, demonstrating that the rigid filler particles enhanced the material's resistance to deformation. The increase in G′ indicates a moderate improvement in elastic response resulting from interactions between the alumina particles and the polymer matrix. Nevertheless, G″ remained substantially greater than G′, confirming that viscous behavior continued to dominate the rheological response. The fluctuations observed in the low G′ values of both the neat resin and the reinforced formulations are likely associated with the limited elastic contribution of the uncured system. At such low storage modulus values, minor variations in oscillatory measurements become more apparent because of increased sensitivity to experimental noise and small material heterogeneities.

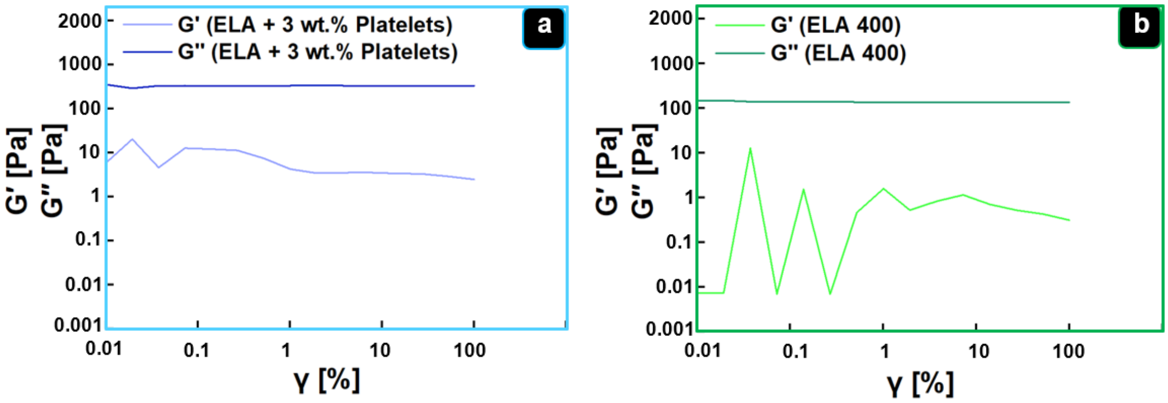

Figure 7: Storage modulus (G′) and loss modulus (G″) as a function of strain amplitude (γ) for (a) ELA400 reinforced with 3 wt.% alumina platelets and (b) ELA400. Rheological values correspond to representative measurements for the printed compositions.

Representative complex viscosity curves for neat ELA400 resin and alumina-reinforced suspensions containing platelet-shaped and CT3000SG alumina particles at various filler loadings are shown in **Figure 8**. For both filler morphologies, the complex viscosity increased progressively with increasing alumina concentration. The suspensions reinforced with platelet-shaped alumina exhibited consistently higher viscosity values than the corresponding CT3000SG formulations, particularly at elevated filler loadings. This behavior is attributed to the high aspect ratio of the platelets, which promotes greater particle-particle interactions and restricts flow. In comparison, the neat ELA400 resin displayed the lowest viscosity throughout the investigated oscillatory strain range, reflecting the absence of solid reinforcement.

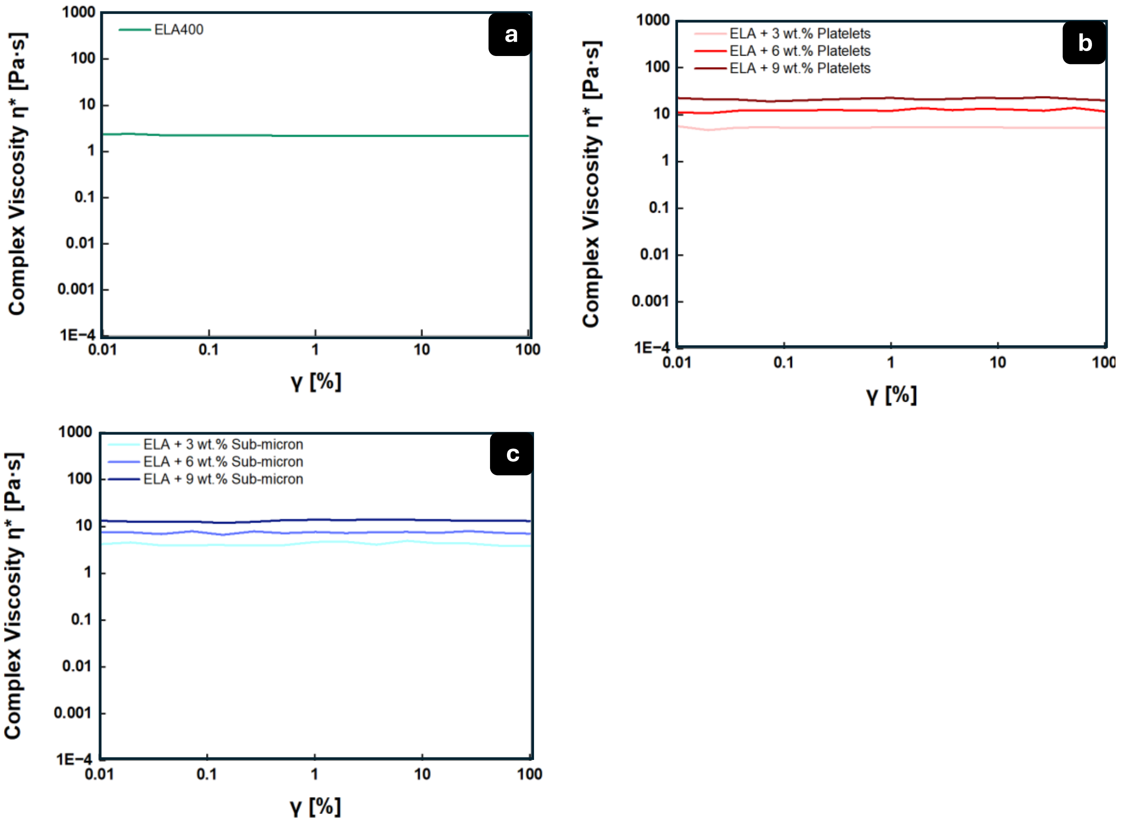

Figure 8: Complex viscosity curves of VPP-processed elastomer samples: (a) without reinforcement, (b) reinforced with 3 wt% - 9 wt% alumina platelets and (c) reinforced with 3 wt% - 9 wt% CT3000SG. Values are presented as representative rheological results for the corresponding compositions.

The increase in viscosity resulting from alumina incorporation is expected to affect the processing characteristics of VPP resins (**Table 2**). Elevated viscosity may hinder the removal of entrapped air bubbles, potentially increasing porosity, and can also reduce light penetration because of enhanced scattering by the ceramic particles. These processing effects are consistent with the differences in porosity and mechanical performance observed between the platelet-reinforced and sub-micron alumina composites. It should be emphasized that the present rheological investigation was limited to oscillatory strain-dependent viscoelastic measurements. Since steady-shear experiments were not conducted, the study does not provide sufficient evidence to evaluate shear-thinning behavior or flow-induced particle alignment. Consequently, all viscosity values reported in this work correspond to the measured complex viscosity (η*).

Table 2: Rheological properties of platelet and sub-micron alumina reinforcements.

Compositions	Storage Modules (G′) [Pa]	Loss Modulus (G″) [Pa]	Complex Viscosity (η*) [Pa·s]
ELA400	0.2 ± 0.1	13.9 ± 0.4	2.2 ± 0.1
ELA + 3 wt.% Platelets	0.6 ± 0.2	33.2 ± 2.2	5.3 ± 0.1
ELA + 6 wt.% Platelets	1.2 ± 0.6	69.3 ± 2.4	11.6 ± 0.1
ELA + 9 wt.% Platelets	2.2 ± 0.6	113.4 ± 2.9	20.2 ± 3.4
ELA + 3 wt.% Sub-micron	0.4 ± 0.1	27.9 ± 0.9	3.9 ± 0.1
ELA + 6 wt.% Sub-micron	0.7 ± 0.1	44.7 ± 2.1	7.1 ± 0.6
ELA + 9 wt.% Sub-micron	1.4 ± 0.3	80.3 ± 3.2	13.1 ± 0.1

* Values are presented as representative rheological results for the corresponding compositions.

3.4 The Microstructural Properties of the Composites

XRD revealed the characteristic reflections of the alumina phase α and alumina reinforcement (**Figure 9**). Across both morphologies, increasing the alumina content from 3 wt.% to 9 wt.% resulted in a clear rise of the integrated corundum peak areas, consistent with the larger crystalline volume fraction. No additional peaks or systematic peak shifts were observed, indicating that neither VPP nor the post-cure transformed the alumina phase. In the CT3000SG system, sharper and taller corundum peaks were observed, reflecting larger coherent domains and lower microstrain of the sintered grains. In contrast, the platelet-filled composites showed broader reflections and slightly altered intensity ratios, which is consistent with the nanoscale platelet thickness and mild preferred orientation induced by flow during printing.

The preferred orientation parameter P was determined from the ratio ΣI(00l)/ΣI(hkl), where ΣI(00l) represented the summed integrated intensities of the preferred α-alumina basal reflections and ΣI(hkl) corresponded to the summed integrated intensities of all detected α-alumina reflections in the measured diffraction pattern. The preferred α-alumina reflections considered for the LF calculation corresponded to diffraction peaks located at 2θ values of approximately like 25.6°, 35.6° and 76.5°. Increasing the alumina loading from 3 wt.% to 9 wt.% resulted in progressively higher total α-alumina diffraction intensities because of the increased crystalline ceramic fraction within the composites. For each alumina morphology, the untreated raw α-alumina powder diffraction pattern was used as the oriented reference baseline for determination of P_0 prior to resin incorporation and printing. Accordingly, P_0 was calculated using the same $\Sigma I_0(00l)/\Sigma I_0(hkl)$ relationship from the raw powder diffraction data representing statistically random α-alumina crystallographic orientation. The LF values were subsequently calculated using the conventional Lotgering relationship, $LF = (P - P_0)/(1 - P_0)$, resulting in LF values of 0.45, 0.43, and 0.55 for the 3 wt.%, 6 wt.%, and 9 wt.% platelet-filled composites, respectively. The substantially higher LF values observed for the platelet-filled systems relative to the sub-micron alumina systems indicated the presence of preferential orientation associated with the platelet morphology during VPP processing.

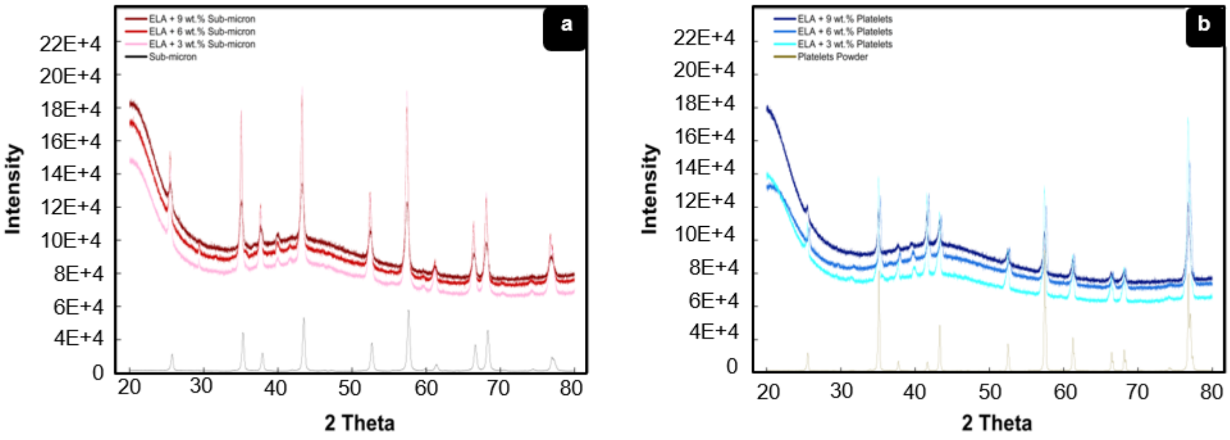

Figure 9: XRD patterns of alumina powders and ELA400 composites containing 3 wt.%–9 wt.% alumina: (a) CT3000SG and (b) platelet-shaped alumina. No significant changes in the characteristic diffraction peaks were observed compared with the corresponding raw powders. The presented XRD patterns and Lotgering factor calculations were obtained from representative measurements of the printed composite specimens.

The porosity of the alumina reinforcements was calculated

Table *3*. In the platelet-filled compositions, the overall porosity remained low, with only a slight increase as the filler content increased. Specifically, the porosity increased from 0.7% ± 0.8% at 3 wt.% to 1.8% ± 0.5% at 9 wt.%. These values are comparable to or even lower than those of the ELA400 reference, indicating that the incorporation of platelets does not significantly promote void formation during processing. Notably, the lowest porosity was observed at 3 wt.% suggested that a small addition of platelets may enhance packing efficiency and resin wetting, thereby reduce trapped air and improve consolidation. In contrast, the sub-micron alumina composites consistently exhibited higher porosities across all concentrations, increasing progressively from 1.7% ± 0.4% at 3 wt.% to 2.5% ± 0.7% at 9 wt.%. This trend demonstrated that finer particles are more prone to generating or retaining voids, likely due to increased slurry viscosity, particle agglomeration, and reduced resin mobility during curing. Such effects can hinder bubble escape and lead to greater void entrapment than in platelet systems. The systematically higher porosity of the sub-micron composites relative to both the neat resin and platelet-filled samples underscores the strong influence of particle morphology on defect formation [63,64].

The Lotgering factor results revealed via **X**-**R**ay **D**iffraction (XRD) a distinct variation in the particle behavior within the resin between the two types of alumina. Higher values were observed when platelets were used, suggesting a stronger alignment of the particles during processing.

This alignment intensified with an increase in platelet content, with values rising from approximately 0.45 at 3 wt.% to over 0.55 at 9 wt.% platelet content. Conversely, almost no orientation was detected for CT3000SG, as its Lotgering values remained approximately zero across all loadings. These findings illustrated that particle shape significantly influences orientation: the flat, flaky structure of the platelets naturally promotes alignment, whereas the CT3000SG powder remained randomly distributed. The data suggested that platelets form a more organized and directional microstructure, whereas sub-micron particles yield a uniform and isotropic mixture [59–61].

Table 3: Lotgering factor and porosity values of platelet-shaped and sub-micron alumina-reinforced composites at concentrations of 3 wt.%, 6 wt.%, and 9 wt.%.

Compositions	Lotgering factor	Porosity
ELA400	-	1.2% ± 0.7%
ELA + 3 wt.% Platelets	0.45	0.7% ± 0.8%
ELA + 6 wt.% Platelets	0.43	1.6% ± 0.8%
ELA + 9 wt.% Platelets	0.55	1.8% ± 0.5%
ELA + 3 wt.% Sub-micron	0.00	1.7% ± 0.4%
ELA + 6 wt.% Sub-micron	0.06	2.2% ± 0.4%
ELA + 9 wt.% Sub-micron	0.03	2.5% ± 0.7%

* Porosity values are presented as mean ± standard deviation from three independently fabricated specimens (n = 3). XRD/Lotgering factor values correspond to representative measurements for the printed compositions.

3.5 The particle morphology of the Composites

The SEM micrograph of the platelet-reinforced ELA composite, in which platelet-shaped alumina particles were observed to be embedded within the polymer matrix with a preferential in-plane orientation (**Figure 10 a**). The flat, flaky morphology of the platelets promoted their alignment during the processing and curing steps, as evidenced by their elongated contours lying predominantly parallel to the surface. This microstructural observation was consistent with the Lotgering factor results, where significantly higher orientation values were obtained for platelet-filled systems. The Lotgering factor increased from approximately 0.45 at 3 wt.% to over 0.55 at 9 wt.%, indicating that particle alignment was progressively enhanced with increasing platelet content.

The bottom-up printing configuration and coordinate system used during fabrication, which played a key role in governing the observed particle behaviour (**Figure 10 b**). The printing direction was oriented along the *z*-axis, while the *xy* plane defined the layer deposition direction. During the bottom-up printing process, shear forces and resin flow induced by the upward movement of the build platform promoted the reorientation of anisotropic platelet particles parallel to the printing plane, thereby enhancing their alignment. This processing-induced alignment mechanism explained the higher Lotgering factors measured for platelet-reinforced composites. In contrast, the nearly CT3000SG particles were not significantly affected by the printing-induced flow field and therefore remained randomly oriented within the resin. The combined SEM, schematic, and Lotgering factor results demonstrated that the interaction between particle shape and printing kinematics controlled the development of either a directional microstructure in platelet-filled composites or an isotropic microstructure in CT3000SG systems.

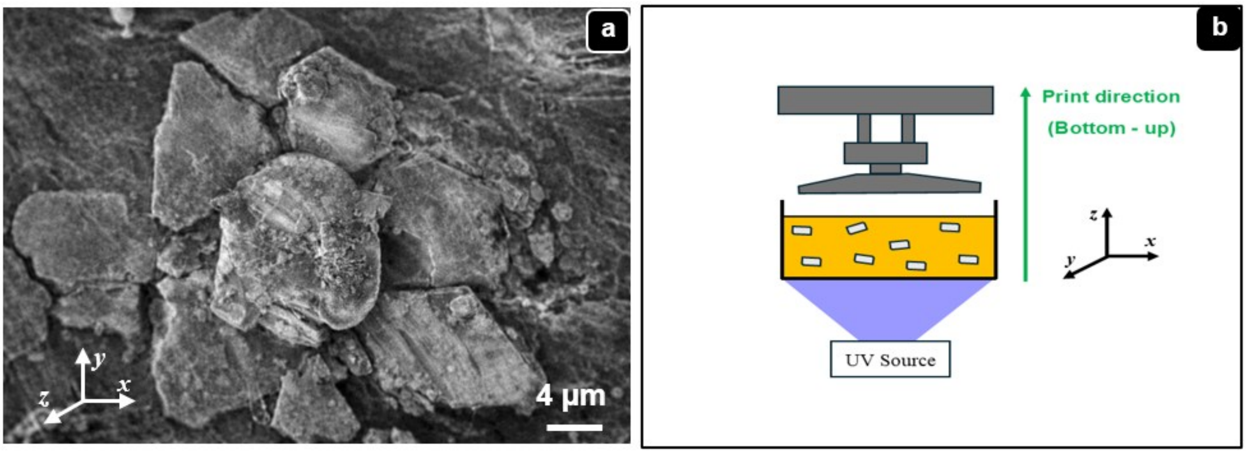

Figure 10: (a) SEM micrograph of a 3 wt.% platelet-reinforced composite showing preferential particle orientation within the photocurable resin matrix; and (b) schematic illustration of the bottom-up vat photopolymerization process.

Representative SEM micrographs of the elastomer composite reinforced with 3 wt.% platelet-shaped alumina are shown in **Figure 11 a** Figure S4a. The images indicate a relatively uniform distribution of alumina platelets throughout the polymer matrix, with several particles displaying preferential in-plane orientation parallel to the printing direction. This microstructural arrangement is consistent with the higher Lotgering factor values and enhanced tensile properties measured for the 3 wt.% platelet formulation. Furthermore, no significant agglomeration or phase separation was detected within the examined regions, suggesting that the particles were successfully dispersed and incorporated during the VPP process.

Representative SEM micrographs of the elastomer composite containing 9 wt.% platelet-shaped alumina are presented in **Figure 11 b**. A high density of platelet particles was observed throughout the matrix, accompanied by localized clustering in certain regions due to the increased filler content. Similar to the lower loading, many platelets exhibited preferential in-plane alignment along the printing direction, in agreement with the orientation trends identified by XRD and Lotgering factor analysis. However, the higher particle concentration promoted stronger particle-particle interactions and a less homogeneous dispersion state, which may have contributed to the reduction in ductility and the earlier onset of fracture observed at elevated platelet loadings.

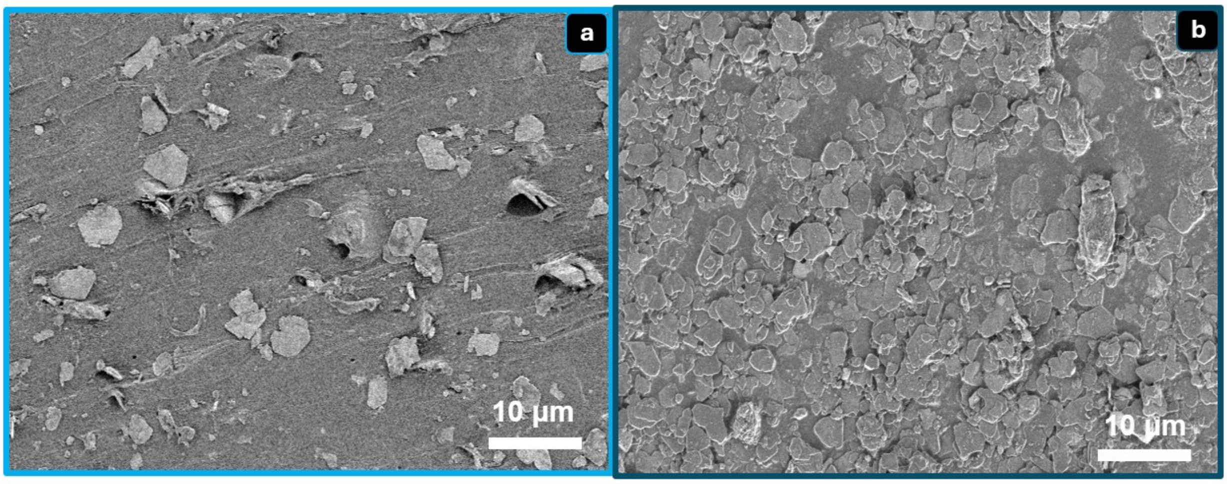

Figure 11: Representative SEM micrographs of platelet-reinforced elastomer composites showing platelet distribution within the polymer matrix: (a) 3 wt.% platelet composite and (b) 9 wt.% platelet composite. The micrographs suggest preferential in-plane platelet arrangement along the printing direction, while increased particle clustering is observed at higher filler loading.

Representative SEM micrographs of the fracture surface of the 9 wt.% platelet-reinforced elastomer composite following tensile failure are shown in **Figure 12 a**. The fracture surface exhibited a high concentration of platelet-rich regions dispersed throughout the polymer matrix, together with a rough and complex crack morphology. The tortuous fracture paths suggest that the presence of platelet-shaped fillers influenced crack propagation by promoting crack deviation within the elastomer matrix. In several areas, the layered microstructure appeared to reflect the preferential in-plane alignment of the platelets induced during the VPP fabrication process.

Higher-magnification SEM images revealed evidence of localized platelet pull-out, interfacial debonding within the fractured regions. These observations suggest that the platelet reinforcements may enhance energy absorption during fracture through filler–matrix interactions and the generation of more tortuous crack paths (**Figure 12 b**). Nevertheless, localized agglomeration and increased platelet–platelet contact were also observed at the 9 wt.% filler loading. Such features may act as stress concentration sites, thereby contributing to the reduced elongation at break and the earlier fracture observed for composites containing higher platelet contents.

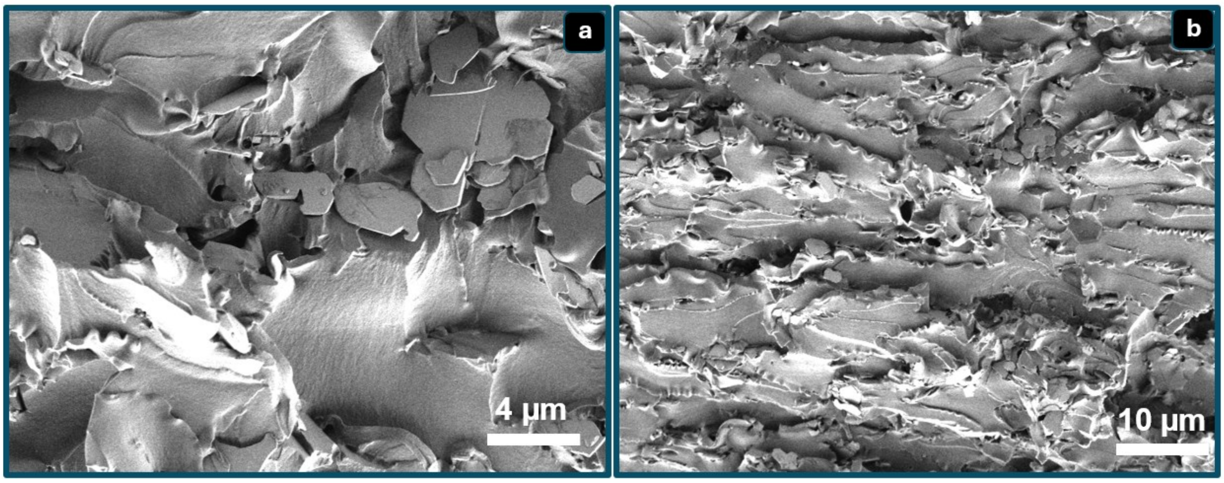

Figure 12: **Representative fracture surface SEM micrographs of the 9 wt.% platelet-reinforced elastomer composite after tensile failure: (a) low-magnification fracture morphology showing platelet-rich regions and tortuous crack propagation paths and (b) higher-magnification image revealing localized particle-matrix separation features.**

3.6 Mechanical Performance of Alumina-Reinforced Elastomer Composites

The tensile behavior of two alumina reinforcements is depicted in **Figure 13**, which illustrated the stress-strain curve alongside the corresponding deformation stages. An incremental increase in tension, beginning with an initial elastic region (stage 1) and transitioning smoothly into nonlinear deformation (stage 2). Further stretching resulted in significant strain accommodation, with the material demonstrating the capacity to endure substantial elongation before attaining its maximum tensile load (stage 3). Final failure was observed shortly thereafter, as evidenced by the abrupt decline in the curve and the fracture captured in stage 4. The smooth, continuous stress–strain curves and progressive necking observed in the sequential images suggest that failure is not governed by sudden crack initiation or brittle defects but rather by uniform plastic deformation of the matrix. Although the reinforced samples exhibited slightly higher porosity, the deformation remained homogeneous, and no premature fracture was observed, indicating that these pores were small, isolated, and non-critical. Consequently, the presence of limited porosity does not significantly deteriorate the tensile strength or elongation, allowing the composites to maintain mechanical performance comparable to or better than that of the neat resin. More importantly, the improved performance of the platelet-filled composite was strongly associated with particle morphology and orientation, as confirmed by the higher Lotgering factor. Increased Lotgering values indicate pronounced platelet alignment during processing, which promotes directional load transfer and creates a more efficient stress-bearing network within the matrix. This particle orientation enhances the packing efficiency, reduces ineffective stress pathways, and facilitates stronger particle-matrix interfacial bonding, thereby compensating for the modest increase in porosity. In contrast, systems with negligible Lotgering factors (randomly oriented particles) lack this reinforcement efficiency. Therefore, the combination of controlled low porosity and strong platelet alignment (high Lotgering factor) showed why the composites exhibit superior tensile behavior despite having a slightly higher void content than pure ELA400.

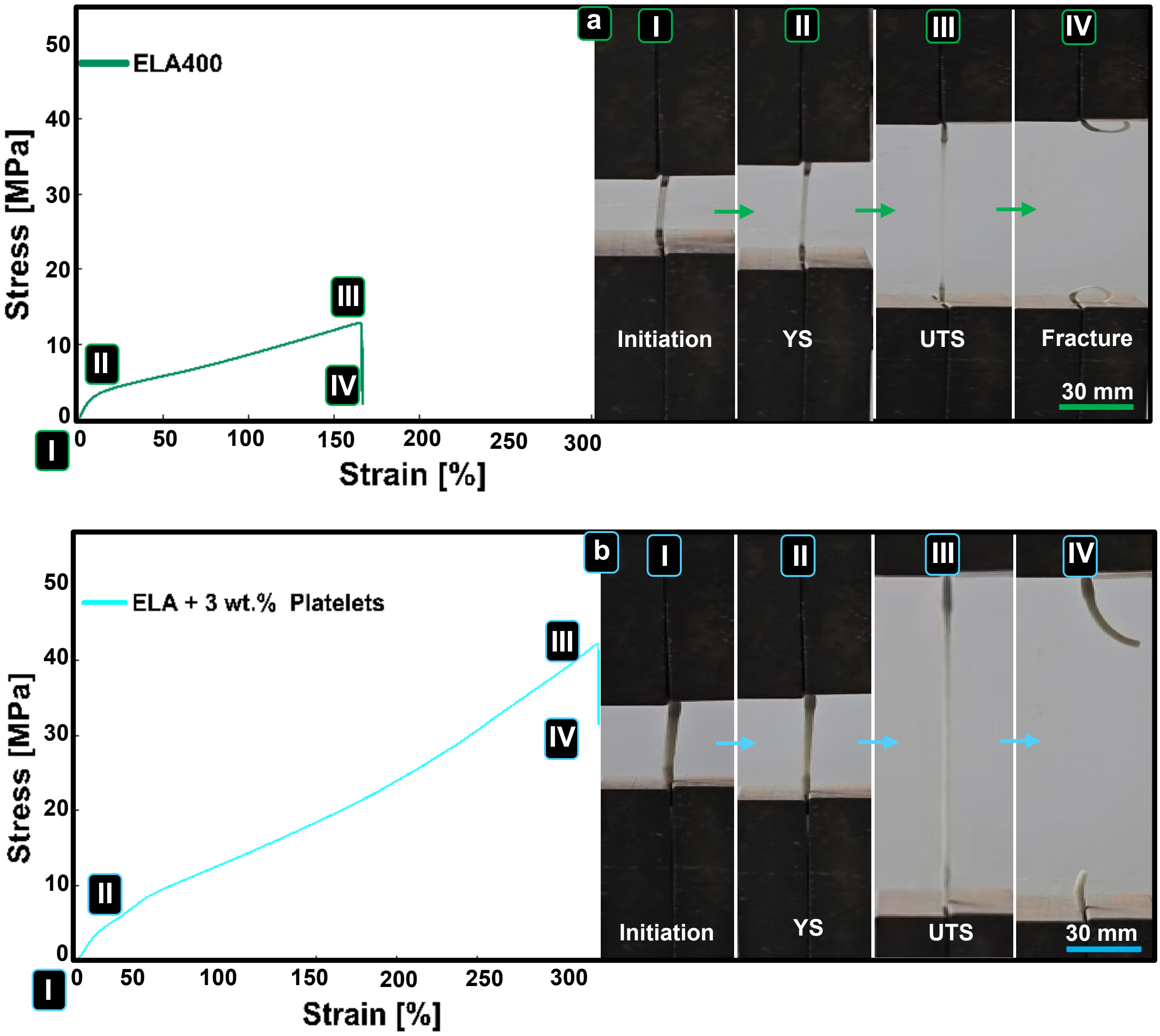

Figure 13: Representative stress–strain curves illustrating the four characteristic stages of tensile deformation: (I) loading initiation, (II) yielding, (III) ultimate tensile strength, and (IV) fracture. The stages are shown for (a) neat ELA400 and (b) ELA400 reinforced with 3 wt.% platelet-shaped alumina. Mechanical properties were calculated from three independently fabricated specimens (n = 3) and are reported as mean ± standard deviation in Table 4.

The 3 wt.% platelet formulation exhibited the most advantageous balance between tensile strength and ductility, characterized by significant strain hardening and sustained load-bearing capacity at large strains. This superior performance was attributable to its low porosity, minimal particle agglomeration and relatively high Lotgering factor, which signified effective platelet alignment within the matrix. At this concentration, the platelets were well dispersed and oriented along the processing direction, facilitating efficient stress transfer across the particle-matrix interface while enhancing packing efficiency and resin wetting, thereby limiting void formation. In contrast, increasing the platelet content to 6 wt.% and beyond results in reduced elongation and earlier fracture despite higher stiffness. This deterioration is due to increased agglomeration, slightly higher porosity, reduced cure depth, and greater density of particle-matrix interfaces, which collectively introduce stress concentrations and serve as crack initiation sites. Consequently, the system transitioned from effective reinforcement to localized embrittlement, diminishing the benefits of platelet alignment at higher loadings. Conversely, sub-micron alumina systems provide only moderate improvements in stiffness and strength, with performance consistently lower than that of platelet-reinforced composites, even at their optimal loading. The nearly isotropic distribution and lower aspect ratio of the sub-micron particles primarily increase the viscosity and promote agglomeration without forming an effective reinforcing network, thereby restricting their contribution to toughness and strength. Additionally, specimens containing 3 wt.% platelets printed in the vertical orientation exhibited lower tensile strength and earlier failure compared to in-plane samples, as weaker interlayer bonding, cure gradients, and defect alignment along layer interfaces amplify the influence of pores and microstructural discontinuities (**Figure** *14*).

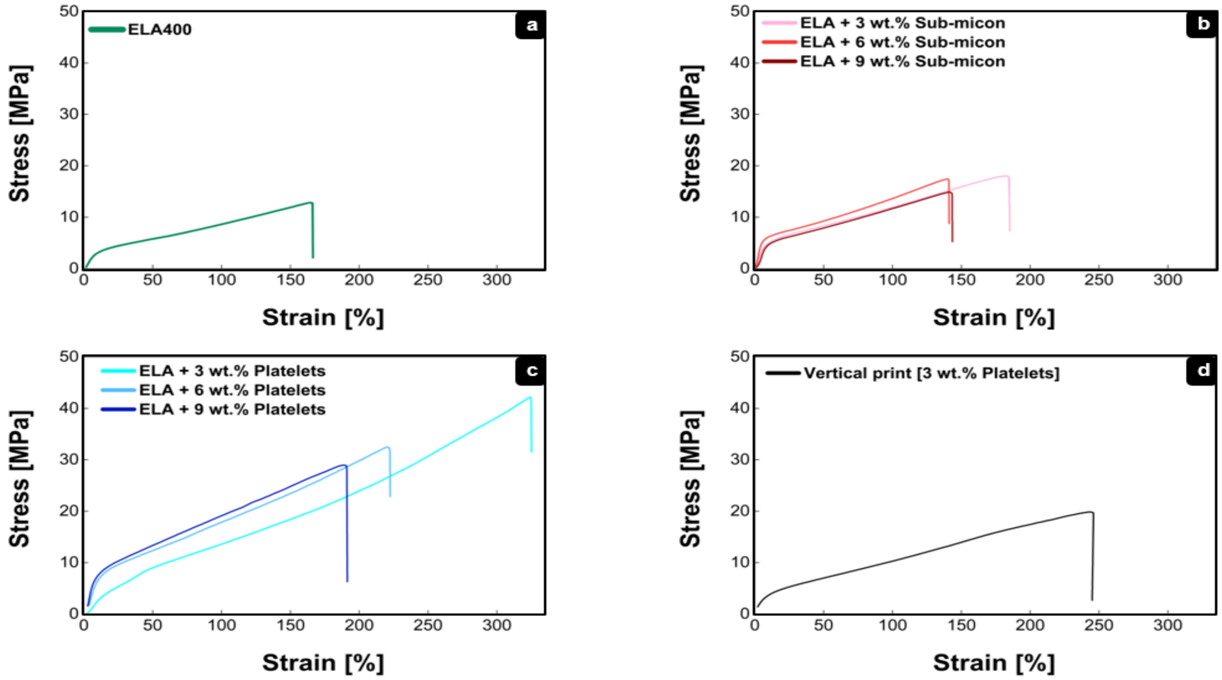

Figure 14: Mechanical properties of VPP-processed elastomer samples with and without alumina reinforcements with concentrations 3 wt.% - 9 wt.%. Representative tensile curves are shown. Mechanical properties were calculated from three independently fabricated specimens (n = 3) and are reported in Table 4 as mean ± standard deviation.

The tensile properties of the neat ELA400 resin are summarized in Table 4**Table *5***, with a **Y**ield **S**trength (YS) of 3.0 MPa ± 0.5 MPa, an **U**ltimate **T**ensile **S**trength (UTS) of 13.0 MPa ± 0.5 MPa and elongation in fracture of 160.0% ± 14.0%. Notable improvements were observed with the incorporation of platelet Al_2O_3. At a 3 wt.% loading, the composite achieves an YS of 7.0 MPa ± 1.0 MPa, a UTS of 45.0 MPa ± 0.8 MPa and an elongation of 310.0% ± 10.0%. As the platelet concentration increased, a diminishing effect was observed: the 6 wt. % formulation exhibits a UTS of 33.0 MPa ± 1.5 MPa with 225.0% ± 8.0% elongation, while the 9 wt.% formulation yields a UTS of 29.0 MPa ± 2.5 MPa and 195.0% ± 12.0% elongation. These reductions at higher solid contents are consistent with increased agglomeration, a larger interfacial area and stronger light attenuation during printing, all of which contribute to cure gradients and early damage initiation.

In all samples, hardness increased with alumina addition, with the magnitude of the increase depending on both filler loading and particle morphology. The most pronounced increase was observed for the platelet-reinforced composites, where hardness increased from approximately 16 Shore A at 3 wt.% to about 27 Shore A at 6 wt.% and 35 Shore A at 9 wt.%. These results are attributed to the high aspect ratio and larger interfacial area of the platelets, which more effectively restrict polymer chain mobility and promote load transfer during indentation. The composites containing sub-micron alumina also exhibited increased hardness, with values rising from approximately 21 Shore A at 3 wt.% to 26 Shore A at 9 wt.%. Notably, the 3 wt.% sub-micron formulation exhibited higher hardness than the corresponding platelet-reinforced composite. However, at 6 wt.% and 9 wt.% filler loadings, the platelet-reinforced composites showed greater hardness than the sub-micron formulations. Overall, these results indicate that both filler loading and particle morphology influence hardness development, with platelet-shaped alumina becoming increasingly effective at higher concentrations due to its larger aspect ratio and enhanced particle–matrix interactions.

Table 4: Mechanical properties of VPP-processed elastomer composites with and without alumina reinforcement at concentrations of 3 wt.%, 6 wt.%, and 9 wt.%.

Compositions	YS [MPa]	Elongation in Fracture	UTS [MPa]	Hardness [Shore A]
ELA400	3.2 ± 0.5	160.5% ± 14.5%	12.4 ± 0.5	13.0 ± 1.6
ELA + 3 wt.% Platelets	7.5 ± 1.0	310.8% ± 10.7%	45.7 ± 0.8	15.6 ± 1.2
ELA + 6 wt.% Platelets	7.8 ± 1.8	225.7% ± 8.3%	33.4 ± 1.5	27.3 ± 1.2
ELA + 9 wt.% Platelets	7.6 ± 2.5	195.4% ± 12.0%	29.6 ± 2.5	35.3 ± 0.5
ELA + 3 wt.% Sub-micron	4.1 ± 1.5	185.6% ± 17.5%	18.6 ± 3.2	20.8 ± 1.0
ELA + 6 wt.% Sub-micron	4.3 ± 2.5	145.7% ± 20.6%	17.4 ± 4.5	23.0 ± 1.5
ELA + 9 wt.% Sub-micron	4.5 ± 1.8	145.5% ± 10.3%	15.7 ± 2.5	25.6 ± 1.8
Vertical (ELA + 3 wt.% Platelets)	6.7 ± 2.0	250.4% ± 15.4%	20.3 ± 3.5	14.8 ± 1.8

* Values are presented as mean ± standard deviation from three independently fabricated specimens (n = 3).

The experimental scatter remained relatively limited for most formulations, indicating acceptable repeatability of the manufacturing and testing procedures. The improvements observed for platelet-reinforced composites were substantially larger than the corresponding standard deviations. For example, the ultimate tensile strength increased from 12.4 ± 0.5 MPa for neat ELA400 to 45.7 ± 0.8 MPa for the 3 wt.% platelet formulation. Similarly, strain at break increased from 160.5 ± 14.5% to 310.8 ± 10.7%. These differences greatly exceed the associated experimental variability, supporting the reliability of the observed trends.

The stress-strain of a representative specimen subjected to cyclic tension from 0 MPa to 12 MPa with constant amplitude loading undergoing 100 cycles is depicted in **Figure 15**. The specimen characterized by the stiffest response during the initial loading cycle, followed by subsequent cycles that displayed pronounced hysteresis indicative of energy dissipation, along with a rightward shift of the loop. After the initial conditioning cycles, the loop width became nearly repeatable, suggesting the attainment of a quasi-steady state and the absence of catastrophic damage within the test window. The 3 wt.% platelet formulation exhibits the largest cyclic strain (25.0% ± 5.0%), indicating the most compliant response under repeated loading. As the platelet concentration increased, the peak strain decreased to 11.5% ± 3.0% for 6wt.% and 10.0% ± 5.0% for 9 wt.%. Even lower strains were observed in the sub-micron alumina composites, which reached 9.0% ± 5.0%, 8.0% ± 4.0% and 5.0% ± 4.0% for 3 wt.%, 6 wt.% and 9 wt.% loadings, respectively, reflecting their higher stiffness under the same conditions. The vertically printed 3 wt.% platelet specimens exhibit intermediate strains of 15% ± 5% and 14% ± 5%, consistent with the influence of weaker interlayer bonding on their deformation behavior. The observed reduction in strain with increasing filler content aligns with the development of a progressively more rigid particle network that restricts matrix deformation. The sub-micron alumina composites exhibited the lowest strains, as their particles were more inclined to form three-dimensional flocculated structures with numerous load-bearing contacts.

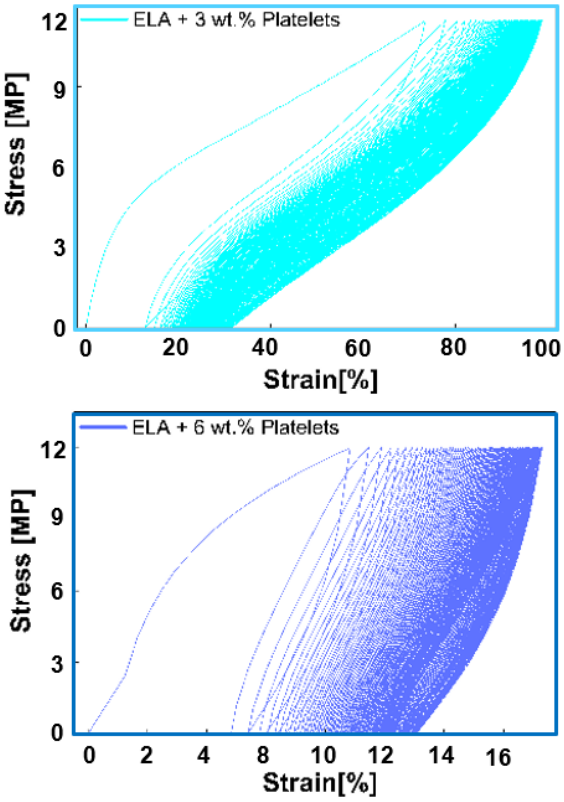

Compositions	Strain
ELA + 3 wt.% Platelets	25.5% ± 5.0%
ELA + 6 wt.% Platelets	11.5% ± 3.4%
ELA + 9 wt.% Platelets	10.3% ± 5.5%
ELA + 3 wt.% Sub-micron	9.6% ± 5.4%
ELA + 6 wt.% Sub-micron	8.5% ± 4.5%
ELA + 9 wt.% Sub-micron	5.8% ± 4.6%
Vertical (ELA + 3 wt.% Platelets)	15.7% ± 5.4%

Figure 15: Representative stress–strain responses of elastomer composites subjected to cyclic loading between 0 and 12 MPa for 100 cycles. The investigated formulations contained alumina loadings of 3 wt.%, 6 wt.%, and 9 wt.%. Strain values were obtained from three independently fabricated specimens (n = 3) and are reported as mean ± standard deviation.

The tensile properties measured after cyclic conditioning are listed in **Table 5**. The 6 wt.% platelet composite achieves the highest UTS of 25.0 MPa ± 2.0 MPa, accompanied by an elongation of 250.0% ± 9.0% and an YS of 6.0 MPa ± 2.8 MPa. The 3 wt.% platelet formulation retains the greatest ductility of 270.0% ± 15.0% but demonstrates a lower UTS of 11.0 MPa ± 2.8 MPa. At 9 wt.% platelets, both strength and elongation diminish (UTS: 16.0 MPa ± 1.5 MPa, elongation: 165.0% ± 7.0%). Orientation effects were also apparent, as vertically printed 3 wt.% platelet specimens display a UTS of 14.0 MPa ± 3.5 MPa with 200.0% ± 15.0% elongation. In the series of platelet-filled composites, the formulation containing 6 wt.% platelets exhibited the highest ultimate strength, approximately 25 MPa, while maintaining significant extensibility, ranging from 240% to 260%. The composite with 3 wt.% platelets retained the greatest ductility, exceeding 250%, but achieved a lower peak stress. Increasing the platelet loading to 9 wt.% results in earlier fracture, occurring at strains between 150% and 170% and a further reduction in peak stress, which is consistent with embrittlement due to particle agglomeration and cure-induced gradients. Vertically printed specimens with 3 wt.% platelets also underperform compared to their in-plane counterparts, failing at lower stresses and strains, a phenomenon attributed to weaker interlayer bonding. In the sub-micron alumina composites, only modest strengthening was observed and the performance ranking reversed with loading. The 3 wt.% micro formulation achieves the highest peak stress, approximately 16 MPa, but at relatively low strains, around 90%, whereas the 6 wt.% and 9 wt.% micro composites sustain larger strains, approximately 160%, but at lower stresses, around 9 MPa. The post- cyclic loading results reflected the balance between cyclic conditioning and the accumulation of damage. Under repeated loading, partial alignment of the platelets can be promoted, enhancing load transfer, an effect that is most beneficial at moderate filler contents, specifically 6 wt.% platelets.

Table 5: Mechanical properties of ELA400 composites reinforced with alumina after 100 cycles of cyclic loading at concentrations of 3 wt.%, 6 wt.%, and 9 wt.%.

Compositions	YS [MPa]	Fracture elongation	UTS [MPa]
ELA + 3% wt. Platelets	**2.0 ± 1.5**	**270.7% ± 15.4%**	**11.0 ± 2.8**
ELA + 6% wt. Platelets	**6.5 ± 2.8**	**250.3% ± 9.6%**	**25.7 ± 2.0**
ELA + 9% wt. Platelets	**5.6 ± 1.7**	**165.4% ± 7.6%**	**16.5 ± 1.5**
ELA + 3% wt. Micro Powder	**4.0 ± 1.5**	**85.5% ± 15.5%**	**16.6 ± 2.5**
ELA + 6% wt. Micro Powder	**5.7 ± 2.5**	**185.6% ± 25.0%**	**8.2 ± 4.3**
ELA + 9% wt. Micro Powder	**5.0 ± 1.8**	**145.3% ± 20.5%**	**10.4 ± 3.0**
Vertical (ELA + 3% wt. Platelets)	**6.5 ± 2.0**	**200.8% ± 15.0%**	**14.0 ± 3.5**

* Values are presented as mean ± standard deviation from three independently fabricated specimens (n = 3).

A similar trend was observed for the second experimental series. Platelet-reinforced composites consistently exhibited superior mechanical performance compared with sub-micron alumina formulations. The magnitude of these differences was generally much larger than the measured standard deviations, indicating that the observed improvements are unlikely to arise solely from experimental scatter. Nevertheless, future studies involving larger sample populations and formal hypothesis testing could further quantify the statistical significance of these differences. A summary of the mechanical properties of the composites is presented in the **Table 6**.

Table 6: Summary of the mechanical performance of alumina-reinforced VPP composites.

Formulation	Hardness	Tensile	Tensile after 100 cycles	cyclic loading strain (0–12 MPa)
ELA400	**Lowest**	**Low strength, very ductile**	**—**	**High (most compliant)**
ELA + 3 wt.% Platelets	**Moderate**	**Best balance: high UTS + very high ductility**	**High ductility; moderate UTS**	**Highest (most compliant)**
ELA + 6 wt.% Platelets	**High**	**High UTS, lower ductility vs 3%**	**Highest post- cyclic loading behavior UTS; good elongation**	**Moderate**
ELA + 9 wt.% Platelets	**Highest**	**Stiff but earlier failure (embrittlement)**	**Lower UTS and elongation**	**Low–moderate**
ELA + 3 wt.% Sub-micron	**Moderate**	**Modest strengthening; moderate ductility**	**Modest UTS; lower ductility**	**Low–moderate**
ELA + 6 wt.% Sub-micron	**Moderate–high**	**Modest UTS; reduced ductility**	**Low UTS; moderate ductility**	**Low (stiff)**
ELA + 9 wt.% Sub-micron	**High**	**Stiff, lowest UTS among filled**	**Low UTS; moderate ductility**	**Lowest (stiffest)**
Vertical (ELA + 3 wt.% Platelets)	**Low–moderate**	**Lower UTS; earlier failure**	**Lower UTS & $\varepsilon_{(}b_{)}$**	**Moderate**

3.7 Discussion

The rheological and mechanical behavior of the alumina-reinforced elastomer composites can be interpreted by considering the combined effects of particle morphology, dispersion quality, and process-induced microstructural features. The increase in complex viscosity with increasing filler content indicates stronger particle–particle interactions, which can adversely affect resin flow during processing. This effect is particularly important in vat photopolymerization (VPP), where resin flowability governs layer recoating and curing uniformity [54]. In addition, the presence of alumina particles increases light scattering within the resin, thereby reducing the effective curing depth and potentially promoting incomplete polymerization and porosity at higher filler concentrations [50].

From a mechanical perspective, the superior performance observed at low filler loadings can be attributed to more efficient stress transfer between the elastomeric matrix and the rigid ceramic inclusions. Moreover, platelet-shaped alumina exhibited a tendency to align preferentially during the printing process, which is consistent with the enhanced load transfer behavior reported in previous studies [55–57]. Nevertheless, the extent of particle alignment could not be quantitatively verified beyond the present analysis, and the observed trends should therefore be interpreted with appropriate caution.

Under cyclic loading, the neat ELA400 resin accumulated the greatest strain, reflecting its pronounced viscoelastic response. The incorporation of alumina reduced strain accumulation for both platelet and sub-micron reinforcements, indicating improved resistance to cyclic deformation. The sub-micron systems, particularly at higher loadings, displayed the lowest accumulated strain due to their greater stiffness and reduced deformability. In contrast, the 3 wt.% platelet composite, despite exhibiting the highest tensile strength and elongation under monotonic loading, accumulated more strain during cyclic testing, suggesting greater viscoelastic deformation under repeated loading. Increasing the platelet concentration from 3 wt.% to 9 wt.% progressively reduced strain accumulation, likely because of restricted polymer chain mobility at elevated filler contents.

Compared with previously reported oxide-filled polymer composites, the elastomeric VPP composites developed in this study achieved a unique combination of enhanced strength and retained deformability at relatively low filler loadings. Earlier investigations of alumina-filled epoxy systems primarily reported improvements in stiffness, hardness, and moderate tensile strength within inherently rigid matrices. For example, Yousri et al. reported approximately 16% improvement in tensile strength and 33% enhancement in hardness for Al_2O_3-filled epoxy composites [46], whereas Zhang et al. achieved about 28% tensile strength improvement using silane-modified alumina nanoparticles. However, these systems generally remained brittle because of the rigidity of the polymer matrix and ceramic reinforcement.

Similarly, alumina-reinforced thermoplastics such as PLA, PA12, and polypropylene typically exhibit tensile and flexural strength improvements of approximately 15% - 35%, depending on filler content and polymer type. Petousis et al. demonstrated enhanced tensile and impact properties in alumina-filled PLA and PA12, while Vidakis et al. reported tensile strength improvements of roughly 15–25% in polypropylene/alumina composites produced by fused filament fabrication [55–57]. Nevertheless, these materials generally display stiffness-dominated reinforcement accompanied by reduced ductility at higher filler loadings. In contrast, the present work focuses on elastomeric VPP composites, where preserving flexibility is equally important for applications involving soft and energy-absorbing structures.

The platelet-reinforced composites exhibited substantially greater mechanical enhancement than many previously reported oxide-filled polymer systems. Incorporation of only 3 wt.% platelet alumina increased the ultimate tensile strength from 12.4 MPa to 45.7 MPa, corresponding to an improvement of approximately 269%, while elongation at break increased from 160.5% to 310.8%, representing an enhancement of approximately 94% relative to the neat resin. These improvements suggest that morphology-dependent reinforcement, reduced porosity, and preferential platelet alignment promote more efficient stress transfer without significantly compromising extensibility. Furthermore, unlike many previous approaches that rely on particle surface modification or external alignment techniques, the present strategy achieves substantial reinforcement through direct filler incorporation using a simple and scalable VPP process.

Despite these benefits, mechanical performance declined beyond the optimal filler loading. SEM observations revealed localized particle agglomeration at higher concentrations, which likely generated stress concentrations and promoted premature failure [54]. In addition, increased resin viscosity and reduced curing efficiency at elevated loadings may facilitate defect formation, including voids and incomplete interlayer bonding [50]. Together, these effects reduce structural homogeneity and offset the strengthening contribution of the ceramic reinforcement.

Although platelet-filled composites exhibited consistently higher Lotgering factors than their sub-micron counterparts, the relationship between filler content and preferred orientation was not strictly monotonic. Moreover, increased particle alignment alone did not necessarily result in superior mechanical properties, indicating that orientation is only one of several factors governing reinforcement efficiency. Agglomeration and porosity can negate the beneficial effects of alignment, demonstrating that the overall mechanical response is governed by the balance between morphology-driven strengthening and defect-induced degradation [55–57].

More broadly, the results emphasize the importance of process-induced microstructural evolution in VPP composites. The interplay among resin viscosity, particle mobility, and photopolymerization kinetics ultimately determines the final microstructure [54]. At higher filler loadings, the restricted mobility of particles in the increasingly viscous resin may hinder homogeneous redistribution during recoating and curing, resulting in localized heterogeneity. Interactions between shear flow and curing kinetics may further influence particle arrangement, although these effects were not directly quantified in the present work.

The exceptional improvement observed for the 3 wt.% platelet composite is attributed to the combined effects of preferential platelet alignment, reduced porosity, enhanced interfacial stress transfer, and uniform particle dispersion. Unlike conventional ceramic-filled polymers, where strength enhancement is often accompanied by reduced ductility, the optimized platelet morphology promoted efficient load transfer while minimizing stress concentrations and defect formation, thereby allowing simultaneous improvements in tensile strength and elongation at break.

The large simultaneous increase in ultimate tensile strength and elongation at break for the 3 wt.% platelet composite should be interpreted as the result of several coupled processing and microstructural factors rather than a single mechanism. At this loading, the platelet particles appear to be sufficiently dispersed to promote effective reinforcement without introducing excessive agglomeration or porosity. The relatively low porosity indicates improved consolidation and reduced defect density, while the measured Lotgering factor confirms preferential platelet orientation, which can enhance directional stress transfer within the elastomeric matrix. In addition, the improved optical transmission and sufficient curing depth at low platelet loading likely contributed to better layer integrity and print quality compared with higher filler contents. Therefore, the observed mechanical improvement is likely associated with the combined effects of particle alignment, reduced porosity, adequate curing, improved print quality, and effective filler–matrix load transfer. However, these mechanisms are inferred from the combined SEM, XRD, UV-Vis, porosity, and mechanical results, and further validation through fracture-surface analysis, sub-micron, or micromechanical modeling would be required to isolate their individual contributions.

Overall, the findings highlight the necessity of balancing reinforcement efficiency with defect minimization in particle-filled elastomeric systems. While rigid fillers improve strength through stress-transfer mechanisms, their effectiveness strongly depends on dispersion quality, interfacial adhesion, and defect density [54]. Because soft polymer matrices are particularly sensitive to flaws, even minor agglomeration or porosity can act as critical stress concentrators that limit mechanical performance [50]. Future studies should therefore focus on improving filler dispersion and interfacial compatibility through approaches such as particle surface functionalization, optimized mixing protocols, and tailored photopolymerization conditions.

An important advantage of the proposed methodology is its simplicity. Significant improvements in mechanical performance were achieved through direct incorporation of alumina particles without requiring complex surface treatments, external alignment techniques, or additional processing steps. This demonstrates that a straightforward and scalable fabrication strategy can produce substantial reinforcement, making it attractive for practical applications where processing simplicity, reproducibility, and cost-effectiveness are essential. Ultimately, the results underscore the importance of optimizing filler morphology, dispersion quality, and processing conditions to achieve the best balance between mechanical performance and manufacturability.

3.8 Study Limitations

Several limitations of the present study should be acknowledged. First, the investigation was limited to a single commercial elastomeric photopolymer resin (ELA400). Although the observed trends provide valuable insight into morphology-dependent reinforcement mechanisms, the quantitative results may vary for other elastomeric photopolymers with different curing kinetics, viscosities, and mechanical properties.

Second, only alumina was considered as the reinforcing phase. Other ceramic fillers, including silica, zirconia, hydroxyapatite, and hybrid reinforcement systems, may exhibit different interactions with the photopolymer matrix and could produce different reinforcement efficiencies.

Third, the cyclic assessment was limited to 100 loading cycles and therefore does not represent the long-term durability of the materials. The cyclic loading results should be interpreted as a comparative evaluation of short-term mechanical stability rather than a comprehensive cyclic loading behavior.

Finally, the proposed reinforcement mechanisms were inferred from the combined SEM, XRD, UV–Vis, porosity, and mechanical characterization results. Direct validation of these mechanisms through advanced techniques such as micro-computed tomography, fracture-surface analysis, in-situ mechanical testing, or micromechanical modelling was beyond the scope of the present study.

3.9 Conclusion

This study demonstrated the significant impact of filler particle morphology on the structural integrity and mechanical performance of alumina-filled VPP composites.

SEM and XRD analyses revealed a distinct difference in particle organization between the two systems: the platelet-filled composites exhibited a pronounced preferred orientation, whereas the sub-micron alumina particles were randomly distributed. This behavior was quantitatively confirmed using the Lotgering factor, which reached approximately 0.45 at 3 wt.% platelets, indicating substantial particle alignment even at low loading levels. Porosity measurements further demonstrated that the 3 wt.% platelet formulation exhibited the lowest porosity (~0.7%), which is lower than that of the neat resin (~1.2%) and significantly below that of the sub-micron systems. These findings suggest that platelet morphology enhances packing efficiency and resin wetting, thereby reducing void formation while simultaneously promoting structural alignment and improving consolidation during processing. These microstructural differences directly influence the mechanical behavior of the composites.

The combination of low porosity and high particle alignment (high Lotgering factor) in the platelet systems facilitated more efficient stress transfer and improved interfacial bonding resulting in significantly superior tensile strength, ductility, and cyclic loading behavior compared with sub-micron composites. Lower platelet loadings (3 wt.%) provided the most favorable balance between strength and elongation due to optimal dispersion, minimal agglomeration, and the lowest measured porosity, whereas intermediate loadings (6 wt.%) maximized strength while maintaining acceptable ductility. However, at higher concentrations, particle agglomeration, increased optical attenuation, and reduced cure depth led to a higher defect density and earlier failure, despite the increased alignment. Conversely, sub-micron alumina yielded only modest mechanical improvements because its random orientation, higher porosity, and limited reinforcement efficiency restricted effective load transfer within the matrix.

The combined SEM, XRD, porosity and mechanical analyses confirmed that controlled platelet alignment, along with minimized porosity and good dispersion, are the dominant factors governing reinforcement efficiency, making platelet alumina the most effective strategy for enhancing the structural and mechanical performance of VPP composites. From a practical standpoint, a platelet loading of 3 wt.% is optimal when ductility and printability are prioritized, while 6 wt.% provides the best compromise between strength and cyclic loading behavior.

This study has several limitations. Only one commercial elastomeric resin and one ceramic reinforcement material were investigated, while the filler loading range was limited to 3–9 wt.%. The cyclic mechanical evaluation was restricted to 100 loading cycles and therefore does not represent standardized long-term cyclic loading testing. In addition, no functional soft robotic demonstrator was fabricated, and the proposed reinforcement mechanisms were inferred from experimental observations rather than directly validated through numerical modeling or in-situ characterization. Future work should address these limitations to further validate and generalize the proposed reinforcement strategy.

Conclusions

This thesis investigated the influence of alumina particle morphology on the microstructure and mechanical performance of elastomeric composites fabricated by vat photopolymerization (VPP). Two alumina morphologies were systematically compared under identical processing conditions: platelet-shaped alumina with a high aspect ratio and sub-micron crushed alumina with a low aspect ratio.

The rheological characterization demonstrated that filler morphology strongly influences resin flow behavior and printability. Increasing filler loading increased viscosity for both reinforcement systems, with platelet-shaped alumina exhibiting a greater effect due to its higher aspect ratio and increased particle interactions.

Microstructural characterization revealed significant differences in particle orientation and structural consolidation. X-ray diffraction analysis showed that platelet-shaped alumina exhibited preferential alignment during the layer-by-layer VPP process, while the sub-micron alumina particles displayed substantially lower orientation. Quantitative evaluation using the Lotgering factor confirmed the morphology-dependent alignment behavior. Furthermore, platelet-reinforced composites consistently exhibited lower porosity than their sub-micron counterparts, indicating improved structural consolidation at equivalent filler loadings.

Mechanical testing demonstrated that particle morphology plays a dominant role in determining reinforcement efficiency. The platelet-reinforced composites exhibited superior tensile strength, elongation at break, and cyclic loading behavior compared with the sub-micron alumina formulations. The most significant improvement was obtained at 3 wt.% platelet loading, where the ultimate tensile strength increased from 12.4 MPa for neat ELA400 to 45.7 MPa while simultaneously increasing elongation at break from 160.5% to 310.8%. These results indicate that morphology-controlled reinforcement can improve both strength and deformability, which are often competing properties in elastomeric composite systems.

By combining SEM, XRD, UV–Vis characterization, porosity measurements, rheological analysis, and mechanical testing, this work established quantitative relationships between particle morphology, preferential orientation, porosity evolution, and mechanical performance. The results demonstrate that platelet-shaped alumina provides more effective reinforcement than sub-micron alumina in elastomeric VPP composites due to its ability to achieve preferential alignment while maintaining relatively low porosity.

Although the observed material properties suggest potential applicability in compliant mechanisms, wearable systems, and other advanced engineering applications, no application-specific demonstrators were fabricated or tested in the present study. Therefore, these applications should be regarded as future opportunities rather than experimentally validated outcomes.

The findings of this thesis contribute to the design of high-performance elastomeric composites for additive manufacturing. The developed material concepts may be relevant to a broader range of applications including flexible structural components, compliant interfaces, energy-absorbing structures, protective coatings, wearable technologies, and advanced additive-manufactured composite systems requiring a combination of high deformability and enhanced mechanical performance.

Future Perspectives and Potential Applications

Several opportunities exist for extending the present research:

1. Future studies should investigate additional elastomeric photopolymers to determine whether the morphology-dependent reinforcement mechanisms identified in this work are transferable across different resin chemistries and curing systems.
2. A wider range of filler loadings should be examined to identify the absolute optimum reinforcement concentration and better understand the transition from beneficial reinforcement to agglomeration-dominated behavior.
3. Other ceramic and hybrid reinforcements, including silica, zirconia, hydroxyapatite, graphene-based fillers, and multi-scale reinforcement systems, should be explored to compare their effectiveness with alumina and evaluate potential synergistic effects.
4. Advanced characterization techniques such as micro-computed tomography, fracture-surface analysis, in-situ mechanical testing, and micromechanical modelling should be employed to directly validate the reinforcement mechanisms proposed in this thesis and to quantify the individual contributions of particle alignment, porosity reduction, and filler-matrix load transfer.
5. Long-term durability studies should be conducted using substantially larger cyclic loading counts and application-specific loading conditions to evaluate the reliability of the materials under service environments.

6. The developed composites should be integrated into functional demonstrators, including actuators, compliant mechanisms, flexible structural components, wearable devices, and energy-absorbing systems. Such studies would provide application-level validation of the material concepts established in this thesis and further demonstrate the practical benefits of morphology-controlled reinforcement in elastomeric VPP composites.

References

[1] Miriyev A, Stack K, Lipson H. Soft material for soft actuators. Nat Commun 2017;8. https://doi.org/10.1038/s41467-017-00685-3.

[2] Khalid MY, Arif ZU, Tariq A, Hossain M, Ahmed Khan K, Umer R. 3D printing of magneto-active smart materials for advanced actuators and soft robotics applications. Eur Polym J 2024;205. https://doi.org/10.1016/j.eurpolymj.2023.112718.

[3] Bliah O, Hegde C, Tan JMR, Magdassi S. Fabrication of Soft Robotics by Additive Manufacturing: From Materials to Applications. Chem Rev 2025;125:7275–320. https://doi.org/10.1021/acs.chemrev.4c00749.

[4] Wang K, Pan W, Liu Z, Wallin TJ, van Dover G, Li S, et al. 3D Printing of Viscoelastic Suspensions via Digital Light Synthesis for Tough Nanoparticle–Elastomer Composites. Advanced Materials 2020;32. https://doi.org/10.1002/adma.202001646.

[5] Farid MI, Wu W, Li G, Yu Z. Research on 3D printing composite material mechanical characterization of robust soft-matter robots. International Journal of Advanced Manufacturing Technology 2024;133:4401–14. https://doi.org/10.1007/s00170-024-13725-2.

[6] Liu G, Zhang X, Chen X, He Y, Cheng L, Huo M, et al. Additive manufacturing of structural materials. Materials Science and Engineering R: Reports 2021;145. https://doi.org/10.1016/j.mser.2020.100596.

[7] Della Santina C, Catalano MG, Bicchi A. Soft Robots. Encyclopedia of Robotics, Springer Berlin Heidelberg; 2021, p. 1–15. https://doi.org/10.1007/978-3-642-41610-1_146-2.

[8] Majidi C. Soft Robotics: A Perspective - Current Trends and Prospects for the Future. Soft Robot 2014;1:5–11. https://doi.org/10.1089/soro.2013.0001.

[9] Iida F, Laschi C. Soft robotics: Challenges and perspectives. Procedia Comput. Sci., vol. 7, Elsevier B.V.; 2011, p. 99–102. https://doi.org/10.1016/j.procs.2011.12.030.

[10] Armanini C, Boyer F, Mathew AT, Duriez C, Renda F. Soft Robots Modeling: A Structured Overview. IEEE Transactions on Robotics 2023;39:1728–48. https://doi.org/10.1109/TRO.2022.3231360.

[11] Walker J, Zidek T, Harbel C, Yoon S, Strickland FS, Kumar S, et al. Soft robotics: A review of recent developments of pneumatic soft actuators. Actuators 2020;9. https://doi.org/10.3390/act9010003.

[12] Yasa O, Toshimitsu Y, Michelis MY, Jones LS, Filippi M, Buchner T, et al. An Overview of Soft Robotics. Robotics, and Autonomous Systems Annu Rev Control Robot Auton Syst 2023 2026;52:6. https://doi.org/10.1146/annurev-control-062322.

[13] Song S, Drotlef DM, Paik J, Majidi C, Sitti M. Mechanics of a pressure-controlled adhesive membrane for soft robotic gripping on curved surfaces. Extreme Mech Lett 2019;30. https://doi.org/10.1016/j.eml.2019.100485.

[14] Kastor N, Vikas V, Cohen E, White RD. A Definition of Soft Materials for Use in the Design of Robots. Soft Robot 2017;4:181–2. https://doi.org/10.1089/soro.2017.29012.nka.

[15] Case JC, White EL, Kramer RK. Soft material characterization for robotic applications. Soft Robot 2015;2:80–7. https://doi.org/10.1089/soro.2015.0002.

[16] Stankova NE, Atanasov PA, Nikov RG, Nikov RG, Nedyalkov NN, Stoyanchov TR, et al. Optical properties of polydimethylsiloxane (PDMS) during nanosecond laser processing. Appl Surf Sci 2016;374:96–103. https://doi.org/10.1016/j.apsusc.2015.10.016.

[17] Bhattacharjee N, Parra-Cabrera C, Kim YT, Kuo AP, Folch A. Desktop-Stereolithography 3D-Printing of a Poly(dimethylsiloxane)-Based Material with Sylgard-184 Properties. Advanced Materials 2018;30. https://doi.org/10.1002/adma.201800001.

[18] Kroner E, Paretkar DR, McMeeking RM, Arzt E. Adhesion of flat and structured PDMS samples to spherical and flat probes: A comparative study. Journal of Adhesion 2011;87:447–65. https://doi.org/10.1080/00218464.2011.575317.

[19] Gorissen B, Reynaerts D, Konishi S, Yoshida K, Kim J-W, De Volder M. Elastic Inflatable Actuators for Soft Robotic Applications. n.d.

[20] Fleck E, Sunshine A, Denatale E, Keck C, McCann A, Potkay J. Advancing 3d-printed microfluidics: Characterization of a gas-permeable, high-resolution pdms resin for stereolithography. Micromachines (Basel) 2021;12. https://doi.org/10.3390/mi12101266.

[21] Hao Y, Zhang S, Fang B, Sun F, Liu H, Li H. A Review of Smart Materials for the Boost of Soft Actuators, Soft Sensors, and Robotics Applications. Chinese Journal of Mechanical Engineering (English Edition) 2022;35. https://doi.org/10.1186/s10033-022-00707-2.

[22] Ilievski F, Mazzeo AD, Shepherd RF, Chen X, Whitesides GM. Soft robotics for chemists. Angew Chem Int Ed 2011;50:1890–5. https://doi.org/10.1002/anie.201006464.

[23] Yang Y, Wu Y, Li C, Yang X, Chen W. Flexible Actuators for Soft Robotics. Advanced Intelligent Systems 2020;2. https://doi.org/10.1002/aisy.201900077.

[24] Zhang Y, Li P, Quan J, Li L, Zhang G, Zhou D. Progress, Challenges, and Prospects of Soft Robotics for Space Applications. Advanced Intelligent Systems 2023;5. https://doi.org/10.1002/aisy.202200071.

[25] Wang X, Wei R, Chen Z, Pang H, Li H, Yang Y, et al. Bioinspired Intelligent Soft Robotics: From Multidisciplinary Integration to Next-Generation Intelligence. Advanced Science 2025;12. https://doi.org/10.1002/advs.202506296.

[26] Sarker A, Ul Islam T, Islam MR. A Review on Recent Trends of Bioinspired Soft Robotics: Actuators, Control Methods, Materials Selection, Sensors, Challenges, and Future Prospects. Advanced Intelligent Systems 2025;7. https://doi.org/10.1002/aisy.202400414.

[27] Ganguly S, Margel S. Fabrication and Applications of Magnetic Polymer Composites for Soft Robotics. Micromachines (Basel) 2023;14. https://doi.org/10.3390/mi14122173.

[28] Mohammadi Nasab A, Sharifi S, Chen S, Jiao Y, Shan W. Robust Three-Component Elastomer–Particle–Fiber Composites with Tunable Properties for Soft Robotics. Advanced Intelligent Systems 2021;3. https://doi.org/10.1002/aisy.202000166.

[29] Boddeti N, Van Truong T, Joseph VS, Stalin T, Calais T, Lee SY, et al. Optimal Soft Composites for Under-Actuated Soft Robots. Adv Mater Technol 2021;6. https://doi.org/10.1002/admt.202100361.

[30] Horne J, McLoughlin L, Bury E, Koh AS, Wujcik EK. Interfacial Phenomena of Advanced Composite Materials toward Wearable Platforms for Biological and Environmental Monitoring Sensors, Armor, and Soft Robotics. Adv Mater Interfaces 2020;7. https://doi.org/10.1002/admi.201901851.

[31] Wang Y, Gregory C, Minor MA. Improving mechanical properties of molded silicone rubber for soft robotics through fabric compositing. Soft Robot 2018;5:272–90. https://doi.org/10.1089/soro.2017.0035.

[32] Zheng H, Zhu S, Chen L, Wang L, Zhang H, Wang P, et al. 3D Printing Continuous Fiber Reinforced Polymers: A Review of Material Selection, Process, and Mechanics-Function Integration for Targeted Applications. Polymers (Basel) 2025;17. https://doi.org/10.3390/polym17121601.

[33] Won J, Jang J, Kim H, Choi I, Park S, Park S. Functional Fibers in Soft Robotics: Advances in Material, Structural, and Systemic Tactics. Advanced Robotics Research 2026. https://doi.org/10.1002/adrr.202500209.

[34] Sheng J, Jiang S, Geng T, Huang Z, Li J, Jiang L. Ultrarobust Actuator Comprising High-Strength Carbon Fibers and Commercially Available Polycarbonate with Multi-Stimulus Responses and Programmable Deformation. Polymers (Basel) 2024;16. https://doi.org/10.3390/polym16081144.

[35] Qu J, Cui G, Li Z, Fang S, Zhang X, Liu A, et al. Advanced Flexible Sensing Technologies for Soft Robots. Adv Funct Mater 2024;34. https://doi.org/10.1002/adfm.202401311.

[36] Narayanan P, Pramanik R, Arockiarajan A. Hard magnetics and soft materials—a synergy. Smart Mater Struct 2024;33. https://doi.org/10.1088/1361-665X/ad2bd8.

[37] Le Duigou A, Correa D, Ueda M, Matsuzaki R, Castro M. A review of 3D and 4D printing of natural fibre biocomposites. Mater Des 2020;194. https://doi.org/10.1016/j.matdes.2020.108911.

[38] Liu K, Chen W, Yang W, Jiao Z, Yu Y. Review of the Research Progress in Soft Robots. Applied Sciences (Switzerland) 2023;13. https://doi.org/10.3390/app13010120.

[39] Nguyen KDQ, Crespo-Ribadeneyra M, Picot O, Colak B, Gautrot JE. Ultrafast Photo-Crosslinking of Thiol-Norbornene Opaque Silicone Elastomer Nanocomposites in Air. ACS Appl Polym Mater 2021;3:5373–85. https://doi.org/10.1021/acsapm.1c00440.

[40] Leong WY. Soft Robotics: Engineering Flexible Automation for Complex Environments †. Engineering Proceedings 2025;92. https://doi.org/10.3390/engproc2025092065.

[41] González-Henríquez CM, Sarabia-Vallejos MA, Rodriguez-Hernandez J. Polymers for additive manufacturing and 4D-printing: Materials, methodologies, and biomedical applications. Prog Polym Sci 2019;94:57–116. https://doi.org/10.1016/j.progpolymsci.2019.03.001.

[42] Ávila-López MA, Bonilla-Cruz J, Méndez-Nonell J, Lara-Ceniceros TE. Strong and Lightweight Stereolithographically 3D-Printed Polymer Nanocomposites with Low Friction and High Toughness. Polymers (Basel) 2022;14. https://doi.org/10.3390/polym14173628.

[43] Domun N, Hadavinia H, Zhang T, Liaghat G, Vahid S, Spacie C, et al. Improving the fracture toughness properties of epoxy using graphene nanoplatelets at low filler content. Nanocomposites 2017;3:85–96. https://doi.org/10.1080/20550324.2017.1365414.

[44] Ryu K, Kim J, Choi J, Kim U. The 3D Printing Behavior of Photocurable Ceramic/Polymer Composite Slurries Prepared with Different Particle Sizes. Nanomaterials 2022;12. https://doi.org/10.3390/nano12152631.

[45] Wang M, Fan X, Thitsartarn W, He C. Rheological and mechanical properties of epoxy/clay nanocomposites with enhanced tensile and fracture toughnesses. Polymer (Guildf) 2015;58:43–52. https://doi.org/10.1016/j.polymer.2014.12.042.

[46] Domun N, Hadavinia H, Zhang T, Sainsbury T, Liaghat GH, Vahid S. Improving the fracture toughness and the strength of epoxy using nanomaterials-a review of the current status. Nanoscale 2015;7:10294–329. https://doi.org/10.1039/c5nr01354b.

[47] Xu J, Jia L, Lan Q, Wu D. Enhanced Thermal and Mechanical Properties of Cardanol Epoxy/Clay-Based Nanocomposite through Girard's Reagent. Polymers (Basel) 2024;16. https://doi.org/10.3390/polym16111528.

[48] Kaybal HB, Ulus H, Demir O, Şahin ÖS, Avcı A. Effects of alumina nanoparticles on dynamic impact responses of carbon fiber reinforced epoxy matrix nanocomposites. Engineering Science and Technology, an International Journal 2018;21:399–407. https://doi.org/10.1016/j.jestch.2018.03.011.

[49] Senthil Kumar MS, Sivakumar M, Senthil SM, Rajeshkumar L. Effect of alumina fillers on physical and mechanical properties of luffa/groundnut shell natural fiber reinforced polymer composites. Polym Compos 2024;45:10457–69. https://doi.org/10.1002/pc.28487.

[50] Sabarinathan P, Annamalai VE, Rajkumar K, Vishal K. Effects of recovered brown alumina filler loading on mechanical, hygrothermal and thermal properties of glass fiber–reinforced epoxy polymer composite. Polymers and Polymer Composites 2021;29:S1092–102. https://doi.org/10.1177/09673911211046780.

[51] Rosenberger A, Ku N, Vargas-Gonzalez L, Alazzawi M, Haber R. Rheology and processing of UV-curable textured alumina inks for additive manufacturing. Int J Appl Ceram Technol 2021;18:1457–65. https://doi.org/10.1111/ijac.13784.

[52] Yousri OM, Abdellatif MH, Bassioni G. Effect of Al 2O 3 Nanoparticles on the Mechanical and Physical Properties of Epoxy Composite. Arab J Sci Eng 2018;43:1511–7. https://doi.org/10.1007/s13369-017-2955-7.

[53] Myles A, Griffith A, Riyad MF, Jiao Y, Mahmoudi M, Minary-Jolandan M. 3D-Printed Ceramics with Aligned Micro-Platelets. ACS Applied Engineering Materials 2023;1:1892–902. https://doi.org/10.1021/acsaenm.3c00223.

[54] Parameswaran V, Shukla DK. Evaluation of elastic modulus of epoxy reinforced with 200nm thick alumina platelets through finite element analysis. Materials Science and Engineering: A 2010;527:3792–9. https://doi.org/10.1016/j.msea.2010.03.019.

[55] SHUKLA D, KASISOMAYAJULA S, PARAMESWARAN V. Epoxy composites using functionalized alumina platelets as reinforcements. Compos Sci Technol 2008;68:3055–63. https://doi.org/10.1016/j.compscitech.2008.06.025.

[56] Gupta R, Zafar S. Investigation of mechanical properties of carbon fiber reinforced polymer incorporating alumina at varying compositions using VARIMC process. Discover Polymers 2025;2:20. https://doi.org/10.1007/s44347-025-00032-6.

[57] Derakhshani K, Alimohammadi M, Eslami-Farsani R. The mechanical behavior of silane-modified nano–Al2O3/ basalt fiber/ polymer composite materials. J Mater Sci 2024;59:15270–82. https://doi.org/10.1007/s10853-024-10080-1.

[58] Fu Z, Freihart M, Schlordt T, Fey T, Kraft T, Greil P, et al. Robocasting of carbon-alumina core-shell composites using co-extrusion. Rapid Prototyp J 2017;23:423–33. https://doi.org/10.1108/RPJ-12-2015-0191.

[59] Cullity BD. Elements of x-ray diffraction. Addison-Wesley Publishing Company, Inc.; 1978.

[60] Feret FR, Roy D, Boulanger C. Determination of alpha and beta alumina in ceramic alumina by X-ray diffraction ABSTRACT. n.d.

[61] Furushima R, Tanaka S, Kato Z, Uematsu K. Orientation distribution-Lotgering factor relationship in a polycrystalline material-as an example of bismuth titanate prepared by a magnetic field. n.d.

[62] Nguyen MTH, Kim JH, Jang WT, Jung YJ, Park EJ, Ha TH, et al. Role of GO and Photoinitiator Concentration on Curing Behavior of PEG-Based Polymer for DLP 3D Printing. ACS Omega 2023. https://doi.org/10.1021/acsomega.3c05378.

[63] Ye Z, Hao Z, Dou R, Wang L, Tang W. Innovative ceramic paste for stereolithography additive manufacturing alumina core applied in turbine blade casting. Int J Appl Ceram Technol 2024;21:2824–31. https://doi.org/10.1111/ijac.14737.

[64] Fouly A, Alkalla MG. Effect of low nanosized alumina loading fraction on the physicomechanical and tribological behavior of epoxy. Tribol Int 2020;152. https://doi.org/10.1016/j.triboint.2020.106550.

Publications

M. Barzegar Keyvani, F. Zongwen, R. Göstl, H. Shokri, C. Putignano, G. Percoco, and B. Gökce, ***Additive manufacturing of Alumina-Reinforced Elastomers***, Advanced Engineering Materials journal, **Accepted for publication, DOI: 10.1002/adem.71082.**

Acknowledgments

I extend my deepest and most heartfelt gratitude to my family for their unwavering love, endless support, and countless sacrifices throughout every stage of my academic and personal journey. Their constant encouragement, patience, and belief in my abilities have been the foundation upon which I have built my perseverance and resilience. Without their guidance and unconditional support, this achievement would not have been possible. I will always be profoundly grateful for the values they instilled in me and for standing by my side through every challenge and success.

I would also like to express my sincere and heartfelt appreciation to my fiancée for her boundless love, understanding, patience, and unwavering encouragement throughout this demanding journey. Her confidence in me, especially during the most difficult moments, has been a continuous source of strength, inspiration, and motivation. Her support, kindness, and belief in my potential have played an invaluable role in helping me overcome obstacles and remain committed to achieving this milestone. I am deeply thankful for her companionship and for sharing this journey with me.

I would like to express my sincere gratitude to the Chair of Materials Engineering and Additive Manufacturing (MAM) at the University of Wuppertal for hosting me during my visiting research period. The opportunity to work within such a dynamic and internationally recognized research environment greatly enriched my academic experience and broadened my scientific perspective. I am especially grateful to the members of the MAM research group for their warm welcome, valuable discussions, and continuous

support throughout my stay. Their willingness to share their expertise, provide constructive feedback, and foster a collaborative atmosphere significantly contributed to both my personal and professional development.

My sincere appreciation also goes to the academic and technical staff for granting access to state-of-the-art laboratory facilities and for their assistance with experimental activities. The knowledge gained and the collaborations established during this visiting period have had a meaningful impact on the quality of this research and will continue to inspire my future scientific endeavors. I am deeply thankful for the hospitality, encouragement, and stimulating research environment provided by the University of Wuppertal and the MAM group, which made my visiting period both productive and memorable.

This research was conducted within the framework of the Ph.D. Programme in Mechanical and Management Engineering at Politecnico di Bari. The author gratefully acknowledges the financial support provided by Politecnico di Bari through the funding associated with CUP D93D22001330001, which significantly contributed to the successful completion of this research and the achievement of the objectives of this dissertation.